

Declaration of Work

The C code for the mathematical model used to generate the atrial electrograms was developed by Dr. Jichao Zhao and myself. All simulations for generating the atrial electrograms were done by me. The MATLAB code used to pre-process and visualize the electrograms were written by myself with the assistance of Dr. Jichao Zhao. The Python code for the training and evaluating the machine learning model was written by me. The clinical data used for validation were provided by Stanford University and University Heart Center, Hamburg.



Engineering Science

Part IV Project 2018 – Final Report

**Machine Learning for Analyzing Panoramic Cardiac
Electrograms to Accurately Locate the Substrates of Atrial
Fibrillation**

Author:

Zhaohan Xiong

Supervisor:

Dr. Jichao Zhao

Abstract

Background: Atrial fibrillation (AF) is the most prevalent form of cardiac arrhythmia affecting over 30 million people worldwide, and drastically increases the chance of stroke and heart failure. Catheter ablation has been a promising clinical approach to treat patients with AF by “burning” localized atrial tissue prone to arrhythmia. However, ablation treatments for AF remain suboptimal due to the lack of an effective approach to accurately interpret AF activation patterns and guide ablation. In 2012, a study led by Stanford professor Narayan proposed Focal Impulse and Rotor Mapping (FIRM), a method of accurately localizing AF drivers for terminating AF with high success rates of 80%. This study gained global attention and the organization owning FIRM was sold for USD 250 million in 2014. However, the efficacy of FIRM has been highly questioned as the same results could not be reproduced in other international clinical trials. Therefore, a robust and open-source algorithm for analyzing atrial activation patterns from patients with AF is of high interest.

Methods: Deep learning has become increasingly popular in recent years, however, require large amounts of labeled data for training. To address this, we have developed a 56-layer convolutional neural network (CNN) trained with synthetic data from physiologically accurate atrial models and validated with clinical data to automatically identify and localize AF drivers across atrial tissues. Our CNN architecture consisted of 55 convolutional layers and 1 fully connected layer to extract features directly from raw atrial activation signals in order to target the dominant region sustaining AF at each time step. The time-wise predictions were then collated to produce a density map, from which the AF driving region was identified. Residual connections were employed throughout the proposed CNN, along with batch-normalization, rectified linear activation units and dropout to improve convergence during CNN optimization. Since our approach was end-to-end, no data preprocessing was required, allowing for the prediction of typical patient data in 3 seconds.

Results and Conclusions: Evaluation of our approach on clinical data showed that our CNN obtained an F_1 accuracy of 85% and a mean squared error distance of 4.5mm when localizing AF drivers from atrial tissue sized 120mm \times 120mm. Furthermore, the extensive hyper-parameter tuning experiments demonstrated that our network architecture and parameter choices are optimal for tackling this challenging task. Potentially, the novel approach proposed in this study could lead to the development of more effective clinical methods for targeting AF drivers to guide ablation treatment, improving the success rates of AF termination in patients worldwide.

Acknowledgments

I would like to thank my supervisor Dr. Jichao Zhao for his continuous support for my research project, for his patience, guidance, mentoring and immense knowledge in the field. I would also like to thank Dr. Zhao's post-doctoral student Jieyun Bai, doctoral student Andy Lo, and research assistant Elizabeth Cheng for their assistance during my project. This project was an amazing opportunity to obtain knowledge and experience in the research field of computational atrial electrophysiology and could not have been completed without the guidance and encouragement of Dr. Zhao and his students.

Contents

| | |
|--|----|
| 1. Introduction | 1 |
| 2. Background | 3 |
| 2.1. Potential Mechanisms Sustaining AF | 3 |
| 2.2. Computer Simulation | 3 |
| 2.3. Machine Learning | 5 |
| 2.3.1. Basics of Neural Networks | 5 |
| 2.3.2. Convolutional Neural Networks | 6 |
| 2.3.3. Residual Connections in CNNs | 7 |
| 3. Methods | 9 |
| 3.1. Data Generation | 9 |
| 3.2. Data Labelling | 11 |
| 3.3. Convolutional Neural Networks for AF Driver Localization | 12 |
| 3.4. Evaluation | 14 |
| 3.5. Hyper-Parameter Tuning | 15 |
| 4. Results | 16 |
| 4.1. Optimal Hyper-Parameters | 16 |
| 4.2. AF Driver Localization Results on Synthetic Data | 17 |
| 4.3. AF Driver Localization Results on Clinical Data | 20 |
| 5. Discussion | 22 |
| 5.1. Algorithms for Localizing AF Drivers to Guide Catheter Ablation | 22 |
| 5.2. Study Limitations | 24 |
| 5.3. Future Work | 25 |
| 6. Conclusions | 25 |
| 7. References | 26 |

List of Figures

| | |
|-------------------|----|
| Figure 1. | 3 |
| Figure 2. | 4 |
| Figure 3. | 7 |
| Figure 4. | 8 |
| Figure 5. | 9 |
| Figure 6. | 10 |
| Figure 7. | 10 |
| Figure 8. | 12 |
| Figure 9. | 13 |
| Figure 10. | 19 |
| Figure 11. | 21 |
| Figure 12. | 21 |

List of Tables

| | |
|-----------------------|----|
| Table 1. | 13 |
| Table 2. | 16 |
| Table 3. | 17 |
| Table 4. | 17 |

Abbreviations

| | |
|------|-------------------------------------|
| ADAM | Adaptive Momentum |
| AF | Atrial Fibrillation |
| AP | Action Potential |
| BN | Batch Normalization |
| BOCF | Bueno-Orovio Cherry and Fenton |
| CNN | Convolutional Neural Network |
| CRN | Courtemanche Ramirez and Nattel |
| ECP | Extra-Cellular Potential |
| FIRM | Focal Impulse and Rotor Modulation |
| MSE | Mean Squared Error |
| NeSI | New Zealand eScience Infrastructure |
| ODE | Ordinary Differential Equation |
| ReLU | Rectified Linear Unit |

1. Introduction

Atrial fibrillation (AF), leading to an irregular and rapid heart rate, is the most common form of heart rhythm disturbance and affects over 30 million people worldwide [1]. AF is associated with substantial morbidity and mortality and causes 1 in 5 strokes in people over the age of 60 years [2]. The current overall prevalence of AF is approximately 2% in industrialized countries and is projected to double in the following decades. Ablation is a promising clinical treatment approach in which localized atrial tissues which are prone to arrhythmias are “burned” or “cooled” to terminate AF in patients [3]. Recent advances in the electrophysiological mapping of the atria have allowed accurate visualization of AF electrical activation patterns to improve treatment by guiding ablation [4]. However, current ablation treatments for AF, especially persistent or permanent AF, remain suboptimal due to a lack of fundamental understanding of the underlying mechanisms that sustain AF [5, 6].

The exact mechanisms of AF have been widely debated, and many conflicting hypotheses have been proposed by research groups worldwide [7-12]. In recent years, two prevailing hypotheses have been proposed as the main mechanisms for sustaining AF: *multiple wavelets* and *localized sources*. The multiple wavelet theory suggests that AF is driven entirely by disorganized waves that chaotically collide, combine and divide as they propagate across the atria, generating new waves that perpetuate the process [13]. Conversely, the localized sources theory suggests that AF is driven by dominant regions of organized activity in the form of reentrant circuits and focal impulses, termed as *AF drivers*, which initiates and sustains continuous rhythm disturbances during AF [14-16]. In 2012, the ground-breaking focal impulse and rotor modulation (FIRM) trial conducted by Stanford professor Narayan and colleagues [17] demonstrated the existence of spatially stable reentrant circuits and focal impulses in 97% of the AF patients in the cohort [4]. Their study further proposed a method to accurately localize and target these drivers in a patient-specific manner to achieve an 86% AF termination rate [11, 18, 19]. This was a staggering improvement from the previous 44.9% reported using pulmonary vein isolation alone, a well-established treatment method used ever since 1998 [20, 21]. Several subsequent FIRM-guided trials also showed similar success rates of 70-80% in AF termination after a 1 year follow up [18, 22], sparking global interest in the FIRM method.

However, despite the high treatment success rates proposed in the FIRM trial, promising results could not be reproduced by several independent clinical centers around the world using the FIRM approach [23, 24]. In addition, other studies have reported that no mathematically distinct electrical activity has been observed at FIRM identified sites during manual offline signal processing [23]. Since the FIRM algorithm is heavily commercialized and the details of its exact methodologies have not been disclosed, the validity of the method itself has been put into question. Therefore, there is still an ongoing need for a robust open-source algorithm capable of accurately targeting atrial regions which potentially drive and sustain AF in patients.

The field of machine learning has grown drastically, with breakthroughs occurring mostly in the past decade due to an increase in the availability of data and

computational capabilities. Deep learning is a category of modern machine learning algorithms involving the use of artificial neural networks [25] and has been the dominant driver of machine learning research in the past 6 years. The success of deep learning can be mainly attributed to convolutional neural networks (CNNs) which became popularized in 2012. Since then, CNNs have set state-of-the-art performance in many challenging tasks such as image classification [26], object detection [27] and signal classification [28, 29]. Thus, CNNs provide the ideal foundation for tackling the challenging problem of AF driver localization.

In this report, we propose a robust CNN to accurately classify atrial activation patterns and localize drivers sustaining AF. Our study will leverage established computer models to generate high-quality atrial activation data to overcome the current challenge with the lack of accurately labeled atrial activation datasets. Our study is the first of its kind to propose the use of cutting-edge deep learning algorithms for this challenging task and will provide critical insights into AF driver localization for effective AF termination during ablation, potentially improving AF treatment worldwide.

2. Background

This section presents a brief overview of the potential types of AF mechanisms and their definitions, as well as background information relevant for building the foundation for the methodologies of this study.

2.1. Potential Mechanisms Sustaining AF

Over the years, the exact electrical mechanisms sustaining AF have been widely debated [7-9]. So far, widely accepted mechanisms for driving AF in the atria include localized *reentrant circuits* and *foci*, and non-localized *multiple wavelets* (**Figure 1**) [7]. Reentrants are the mechanism involving electrical waves circulating around an unexcited but excitable tissue [30]. Reentrants which form continuous rotations are often called “reentrant circuits”, or “rotors”, and are one of the most prevailing hypotheses for explaining the source and cause of the disorganized atrial electrical activity during AF. Multiple wavelets are regarded as non-localized and involve irregular waves which collide, combine and divide as they travel across the atria, generating new waves that perpetuate the process [31]. Reentrant circuits have been described as localized sources [14], however, depending on the circumstances, may decompose into increasingly complex patterns to form multiple wavelets [13]. Foci mechanisms are a category of potential AF drivers involving centrifugal electrical waves fired from localized sources. According to studies, foci are unlikely to sustain AF [7] but have been hypothesized to induce abnormal beats and wave breaks in the atria which initiate reentrant circuits or multiple wavelets mechanisms [32].

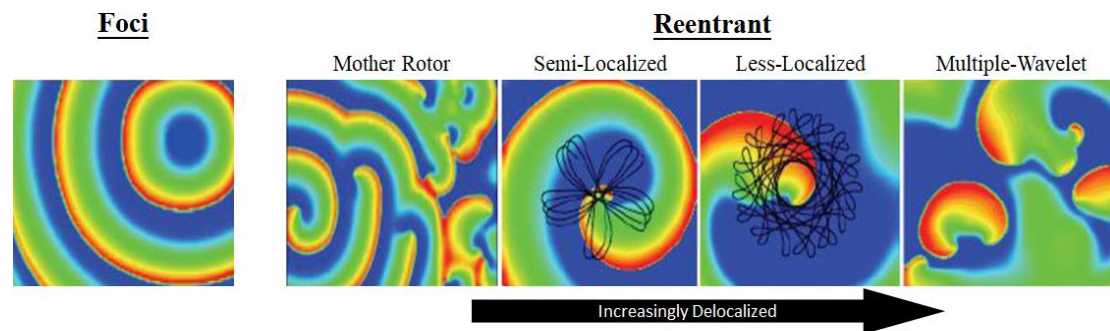


Figure 1. Visualization of the potential mechanisms of atrial fibrillation adapted from Weiss et al. [7]. Typical examples of foci and reentrant circuits (rotor) are shown, along with the subtypes of reentrants. The progression of the rotor from localized to delocalized is shown firstly by the stable mother rotor, secondly and thirdly by the semi-localized rotors which oscillate along the black-lined trajectory, and lastly by the multiple-wavelets mechanism which is completely delocalized.

2.2. Computer Simulation

The underlying mechanisms responsible for AF have been widely studied in silico with mathematical models of the atrial electrophysiology on a cellular, tissue and organ level. The capability to model cellular dynamics under realistic physiological and pathological environments enables investigation of atrial excitation propagation and arrhythmia. In functional atrial cells, an electrical charge is present due to

disparities in the concentration and permeability of ions, resulting in a potential difference being maintained across the membrane [33]. This trans-membrane potential, also known as *action potential* (AP), plays an important role in coordinating the contractions of the atria and has been shown to change significantly during the course of atrial arrhythmias such as AF [34].

In 1998, Courtemanche, Ramirez, and Nattel (CRN) published a pioneering study proposing a model of the human atrial AP, ionic currents and ion concentrations that underlie the electrical properties of the atrial tissue under normal and pathological conditions [35]. The cellular electrical behavior was described with a set of nonlinear-coupled ordinary differential equations (ODEs), taking into account the concentration, currents and binding to intracellular structures of the potassium (K^+), sodium (Na^+) and calcium (Ca^{2+}) ions. The ODEs, or gating variables, control the flow of the various ionic currents through the membrane channels. The formulation was based on clinical data recorded from human atrial myocytes and describes the behavior of inward, outward, delayed, pump, exchangers and background ionic currents in a detailed manner (**Figure 2**). The rate of change of the AP can, therefore, be calculated by summing the individual ionic currents as well as any additional stimulus current and dividing the total by the membrane capacitance.

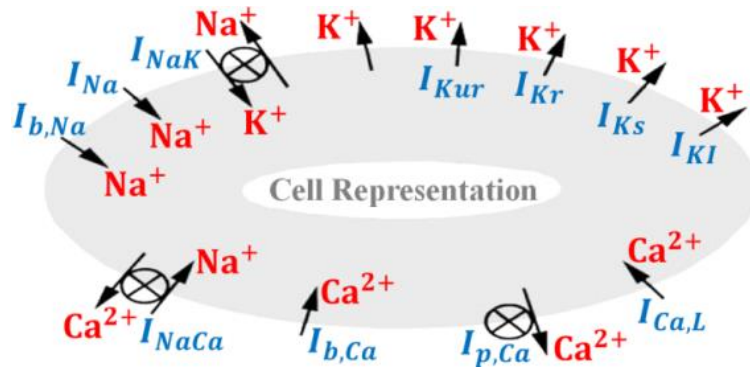


Figure 2. Schematic representation of the currents (I), pumps and exchanges (\otimes) of the atrial model adapted from Courtemanche et al. 1998 [35]. Potassium, K^+ ; Sodium, Na^+ ; Calcium, Ca^+ . Abbreviations of currents: I_{KI} , inward K^+ ; I_{Ks} , slow delayed K^+ ; I_{Kr} , rapid delayed K^+ ; I_{Kur} , ultra-rapid delayed K^+ ; I_{NaK} , Na^+ - K^+ pump; I_{Na} , inward Na^+ ; $I_{b,Na}$, background Na^+ ; I_{NaCa} , Na^+ - Ca^+ exchanger; $I_{b,Ca}$, background Ca^+ ; $I_{p,Ca}$, Ca^{2+} pump; $I_{Ca,L}$, inward Ca^+ .

The formulation of the CRN model, along with many others [36-39], contains a large number of ODEs (21 for the CRN model) which are computationally expensive to solve and the solutions are memory intensive to store. The handling of the considerably large number of parameters for the ion channels also introduces significant inefficiencies. Although these models are capable of describing the effects of specific ionic currents in detail, more simplified models have been proposed focusing predominantly on the spatial-temporal behavior of the atrial AP. In 2008, Bueno-Orovio, Cherry and Fenton (BOCF) proposed a minimalistic model which consists of a reaction-diffusion equation for the AP and was controlled by only 3 gating variables, or ODEs [40, 41]. The substantially smaller number of parameters

makes the modification of the model parameters significantly easier for experimental reproducibility and large-scale high-resolution simulations. Further studies have therefore been conducted comparing the atrial excitation patterns of the detailed CRN model and simplified BOCF model [41-43]. These studies concluded that the main features of the AP during various AF mechanisms could be accurately reproduced with the BOCF model if the study being conducted is purely focused on the spatial-temporal behavior of the atrial electrical propagations and the specific ionic current are of less importance [41]. Since the focus of our study is purely based on the spatial-temporal behavior of the AP, the BOCF model provides the ideal infrastructure for the simulation of a large number of mechanistically different atrial electrograms available for extensive investigation and analysis.

2.3. Machine Learning

2.3.1. Basics of Neural Networks

Machine learning has gained global momentum in recent years for driving the development of more intelligent algorithms to analyze increasingly complex data. Supervised machine learning is a class of algorithms which learns from a given set of data and labels, and is ideal for our study due to the availability of large amounts of synthetic data to maximize its performance. In traditional machine learning algorithms such as support vector machines [44], random forests [45] and K-nearest neighbor [46], a set of features is initially manually generated from the raw data by applying transformations to extract more meaningful information. These features are then fed into a non-linear classifier, whose parameters are then optimized to identify key characteristics of data in different categories. This process requires domain expertise, as a rigorous feature generation and selection procedure is required to find the optimal feature set for learning [47]. Although such methods have been fairly effective, the manual labor required is a major bottleneck for rapid prototyping and driving algorithm performance.

Neural networks are a category of modern machine learning algorithms and have been widely applied in the medical field in recent years [25, 48, 49]. The effectiveness of neural networks lies in their ability to automate the feature generation and selection process [25]. This greatly increases the algorithm's learning efficiency as the entire process is fully data-driven, allowing for an ease of adaptability to a wider range of tasks [48]. Because of this, neural networks have been the dominant driving force of artificial intelligence research in the past decade [26], surpassing human-level performance in many challenging tasks such as facial recognition [50], natural language processing [51], self-driving cars [52], and medical diagnosis [53, 54].

The learning process of neural networks is set up as a non-linear, unconstrained optimization problem. Data is fed into the network through a series of matrix operations, or layers, which performs several weighted function evaluations. The weight parameters are initialized with random values sampled from a distribution of choice, such as a normal distribution [55]. These weights are then optimized such that data are linearly separated at the neural network output, producing different values

depending on the input [25]. An optimization problem can then be formulated to minimize a loss function with gradient descent [56]. For linear regression problems such as time series forecasting [57], object localization [58] and landmark detection [59] where the prediction must be a continuous variable, the most common optimization objective is the mean squared error (MSE):

$$L(f(x), y) = \frac{1}{R} \sum_{i=1}^R \sqrt{(y_i - f_i(x))^2} \quad (\text{Equation 1})$$

which measures the Euclidean distance between the predictions, $f(x)$, and the ground truth, y for the loss, L , evaluated on R output predictions.

The network makes updates to the weight parameters iteratively to improve its performance with backpropagation [60] to better match the provided training data with their ground truths such that

$$\omega^i = \left(1 - \frac{\nu}{N}\right) \omega^i - \nu \frac{\partial L}{\partial \omega^i} \quad (\text{Equation 2})$$

where the weight, ω , at layer i , is updated for a learning rate ν , with a total sample N .

Since the optimization problem is unconstrained, to avoid excessively large numerical values, an activation function, f , is applied to every weight parameter [61]. There are two types of activation functions commonly used in neural networks. The rectified linear unit (ReLU) for values in each layer, l , is defined as

$$f_{ReLU}(l) = \max(l, 0) \quad (\text{Equation 3})$$

and it is used at intermediate layers to increase the speed of convergence during optimization [62]. The outputs for regression problems are continuous and the neural network would contain R output nodes when predicting R variables. To restrict the numerical values of these outputs nodes, the sigmoid activation function

$$f_{Sigmoid}(l_i) = \frac{1}{1+e^{-l_i}}, \forall i \in [1, R] \quad (\text{Equation 4})$$

is used for the i 'th node that the output layer, l , such that their individual values are within $[0, 1]$, representing normalized continuous variables. The output values can then be re-scaled to different magnitudes depending on the regression problem.

2.3.2. Convolutional Neural Networks

CNNs [63], which became popularized in 2012 [26], specialize in image processing, and have obtained state-of-the-art performances in problems such as image classification [26, 64-66], object detection [27] and semantic segmentation [67, 68]. CNNs consist of multiple layers which directly process 2D data with convolution operations (**Figure 3A**), allowing the network to learn spatial relationships within image pixels. The convolution operation is performed by sliding a small filter across the entire input image and calculating the dot product between the input and the filter at each step. This is written as

$$l_{i,j}^{n+1} = f\left(\sum_{a=1}^K \sum_{b=1}^K \kappa_{ab} l_{i+a,j+b}^n\right), \forall i, j \in l^n \quad (\text{Equation 5})$$

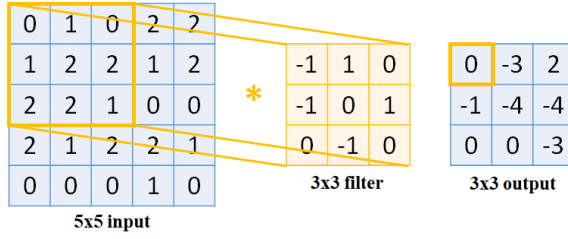
for a $K \times K$ filter, κ , at each (i, j) over the entire input of layer l^n . The values in the

filter are therefore weight parameters to be trained. The entire convolution operation can be repeated F times per layer with different filters to create F feature maps to increase the degrees of freedom for optimization, transforming an $M \times N$ input into an $M \times N \times F$ matrix.

Pooling is another common operation used in CNNs (**Figure 3B**). It increases the efficiency of training by compressing the matrices at certain layers to decrease the computational costs in a network. Max-pooling is the most commonly used type of pooling where a layer is down-sampled by a factor of K through taking the maximum in each $K \times K$ sub-grid, i.e.,

$$l_{i,j}^{n+1} = \max(l_{i+k,j+k}^n), \forall k \in [0, K-1]. \quad (\text{Equation 6})$$

A. Convolution Operation



B. Max Pooling Operation

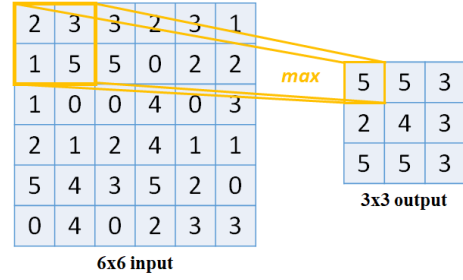


Figure 3. The basic operations in a convolutional neural network. **A)** A simple convolution operation. **B)** A simple max pool operation.

Since CNNs usually contain millions of parameters which have to be optimized, overfitting is a major concern as the network loses its ability to generalize to unseen data [69]. Dropout is a technique which alleviates overfitting by randomly setting network nodes to zero [70]. This forces the CNN to find unbiased features in the dataset that are representative of the data in general, instead of specific characteristics that appear only in the training set. A dropout rate, ϕ , is used such that the layer l^n becomes

$$l_{i,j}^n = l_{i,j}^n \phi_{i,j}^n, \forall i, j \in l^n \quad (\text{Equation 7})$$

where ϕ equals zero with a pre-determined probability.

2.3.3. Residual Connections in CNNs

The optimization of CNNs is a gradient-based method and can be enhanced via the use of residual connections. Residual connections provide an alternative pathway for the gradients to be propagated during backpropagation (**Figure 4**) [66]. The motivation of residual blocks stemmed from an optimization problem which occurred in traditional CNNs which do not contain skip connections. In traditional CNNs, it was observed that by utilizing a larger number of layers, which was previously thought to increase the learning capacity by increasing the degrees of freedom, resulted in a decrease in performance during training compared to CNNs with fewer

layers. The vanishing gradient problem is a possible explanation to this phenomenon, where, in larger CNNs, the gradients of the layers that are deeper in the network progressively approach zero after many iterations due to the repeated derivative calculations in backpropagation, resulting in non-optimization [71]. By preserving the original gradient and combining it with the gradient after the convolution, skip connections can increase the efficiency of the propagation of gradients during weight parameter updates in gradient descent.

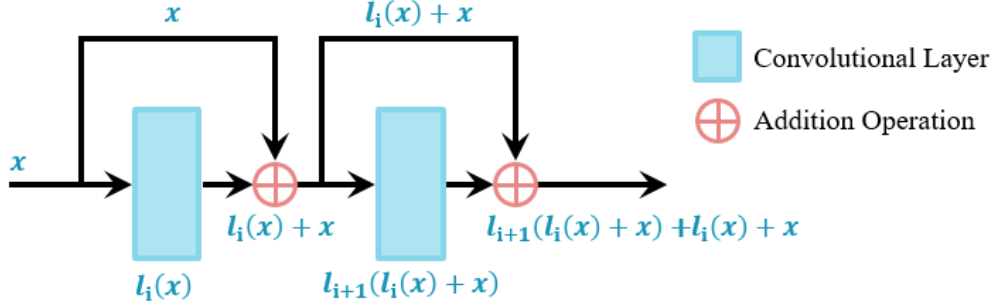


Figure 4. Illustration of the basic operations in residual blocks. The skip connections provide an alternative pathway for information to be propagated without introducing additional parameters. The original input data is merged with its respective transformed version via the use of an element-wise sum.

Within a residual block, a typical network includes a batch normalization (BN) layer, followed by a ReLU layer, and then a convolutional layer [29, 66]. BN is a layer which constantly normalizes each mini-batch throughout the entire network, reducing the internal covariant shift caused by progressive transforms [72]. BN uses the mean of the mini-batch, in a layer, x_{mean} , and their standard deviation, x_{std} , such that

$$BN(l_i) = \gamma \left(\frac{x_i - x_{mean}}{x_{std}} \right) + \beta \quad (\text{Equation 8})$$

where x_i represents entries in the current mini-batch and γ and β are trained parameters. By applying ReLU before a convolution layer, as opposed to applying it after, as in the traditional fashion, the input values are further normalized to accelerate optimization [66].

3. Methods

This section describes the details of the methods used in this study (**Figure 5**). Since CNNs perform best when trained on large labeled datasets, Section 3.1 describes the simulation of a large synthetic dataset. Section 3.2 then describes how labels can be generated in order to train a CNN in a supervised manner. The proposed CNN architecture for AF driver localization is described in Section 3.3, and the evaluation of the network is described in the subsequent Section 3.4. The methods section ends with a description of how the parameters of the proposed network were tuned to ensure optimal performance.

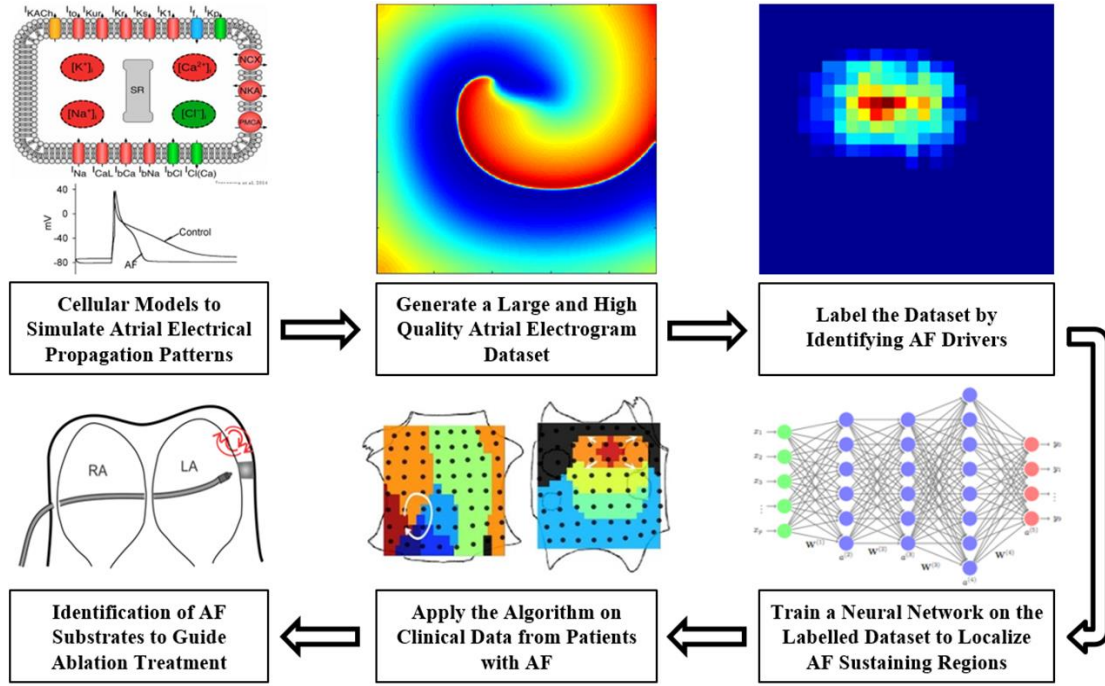


Figure 5. The workflow for the development of a model for automatic AF driver localization.

3.1. Data Generation

The BOCF human cellular model [40] with the parameters given in [73] was used to generate accurate electrical propagation patterns of functionally stable AF drivers in the human atria. The model controlled the total Ca^+ , K^+ and Na^+ ionic currents through each cell with equations of the slow inward current, J_{si} , slow outwards current, J_{so} , and fast inwards current, J_{fi} , respectively. The magnitudes of these three currents were controlled with relaxation times, τ_{si} , τ_{so} and τ_{fi} , to allow the change in the behavior of electrical waves during simulation. The simulations were performed over a 2D area with spatial dimensions of $120\text{mm} \times 120\text{mm}$ for a 10 second time period with different pacing protocols. The size was chosen to approximate that of the atrial surface which has an estimated average length of 120mm [74], and the time was chosen to allow sufficient time for generating stable drivers continuously sustaining AF [75]. The simulations were done by solving the three ODEs in the BOCF model using the forward Euler method [76] with a spatial discretization of $\Delta x = \Delta y =$

0.15mm and a time discretization of $\Delta t = 0.0025\text{ms}$. The APs from the simulations were saved every 400 timesteps, resulting in a sampling frequency of 1000Hz. All simulations were implemented in C and were executed on the New Zealand eScience Infrastructure (NeSI) using parallel computing.

Stable reentrant circuits were generated with the S1-S2 method [77], as shown in **Figure 6**. This was done by first applying an initial stimulus (S1) across a $5\text{mm} \times 120\text{mm}$ region on the left-hand boundary of the tissue. The S1 wavefront propagated to the right-hand boundary, where a second stimulus (S2) was applied on a $60\text{mm} \times 60\text{mm}$ square region in the top left corner of the tissue. Due to the interference of the S1 and S2 waves, the S2 wave was only able to travel downwards, as the S1 wave inhibited its propagation to the right. This resulted in the formation of a rotating wave which formed a stable reentrant circuit after 70ms.

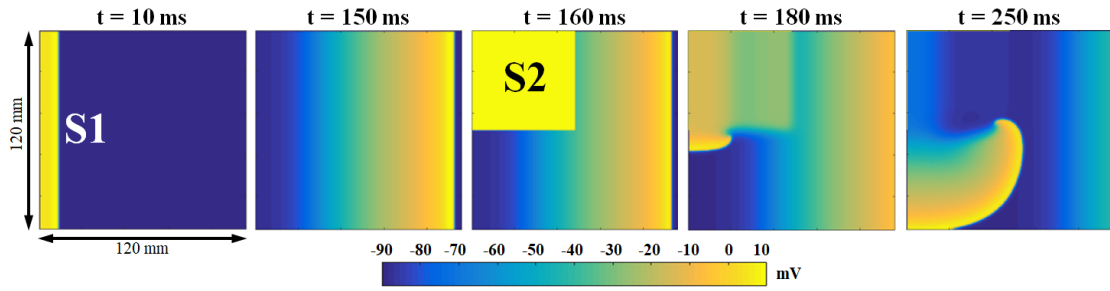


Figure 6. Different snapshots over time of the S1-S2 method for generating the reentrant circuit mechanism. The first stimulus, S1 (at $t = 10\text{ms}$), interferes with the second stimulus, S2 (at $t = 160\text{ms}$), to produce a rotating wave.

The stability of the reentrant circuits was controlled by changing the amount of Na^+ current through each cell. This was achieved by decreasing τ_{fi} to increase the current flow. The default value of τ_{fi} was 0.125 and resulted in a stable reentrant circuit with the center of rotation oscillating near the center of the tissue surface. By progressively decreasing τ_{fi} to a value of 0.015, the precession path of the reentrant circuit centroid became further away from the center of the tissue, resulting in increasingly delocalized reentrant circuits (**Figure 7**). Values of τ_{fi} above 0.15 and below 0.015 caused reentrant circuits to decompose after 1 to 5 cycles, resulting in drivers which do not sustain AF.

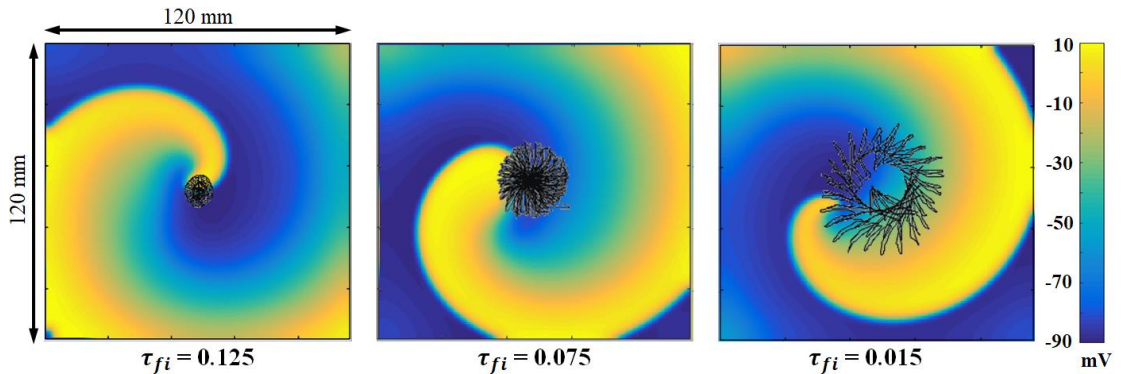


Figure 7. AF sustaining reentrant circuits with different relaxation times (τ_{fi}) for the flow of sodium

current (Na^+) through each cell. The trajectory of the center of rotation is shown by the black line over a 10 second period. Decreasing values τ_{fi} of resulted in increasingly delocalized precession.

The location of the centroid of the reentrant circuits was controlled by first generating a stable reentrant circuit with the S1-S2 method. The solutions of the ODEs at the tissue sub-region containing the centroid were then saved and loaded at different spatial coordinates of an unexcited tissue to create simulations of reentrant circuits at different locations.

Clinical atrial electrograms obtained with constellation basket catheters are of the electrical activation patterns recorded with electrodes placed at a small distance above the atrial tissue [78, 79]. To replicate the environment under clinical settings, the APs generated with the BOCF model were converted to the extra-cellular potential (ECP), Φ , by using the 2D large volume conductor approximation [80]

$$\phi_{x',y',z'} = -K \int \int \nabla V_m \cdot \nabla \frac{1}{r} da \quad (\text{Equation 9})$$

where K is the ratio of the intracellular and extracellular conductivity, ∇V_m is the gradient of the AP across the 2D space, r is the distance from the position of the electrodes (x', y', z') to each point across the tissue (x, y, z), and da is the derivative of the area. 240×240 virtual electrodes (one for each element of the simulation) spaced by 0.5mm with a distance, z' , or 0.5mm above the tissue surface were used for this conversion. Thus, the ECPs of the atrial activation patterns were used as the data for developing the proposed CNN.

3.2. Data Labelling

The AF driver region was automatically computed as the area with the highest density of reentrant circuit centroid, or phase singularity, occurrences over the 10 second time period. This was first done by converting the ECP into a phase map

$$\theta_t = \arctan\left(\frac{-(\phi_t - \phi^*)}{H(\phi_t) - \phi^*}\right) \quad (\text{Equation 10})$$

where H is the Hilbert transform [81], ϕ^* is the origin of the phase plane with respect to the phase being computed, and θ_t is the phase over time, defined as the angle between the original signal and the Hilbert transform of the signal [82]. The phase singularity was then located by identifying all points of the phase map which satisfied the expression

$$\oint \nabla \theta dr = \pm 2\pi \quad (\text{Equation 11})$$

where the line integral around the eight neighboring elements of each element in 2D summed to $\pm 2\pi$. The density was calculated for each 8×8 grid in the 240×240 mesh, producing a smoothed heat map of the phase singularity occurrence (**Figure 8**). A threshold of 40% was used to obtain the sub-regions in which the phase singularity was the most frequent, and this was deemed as the driver sustaining AF. This method of identifying AF drivers followed many past clinical studies which utilized thresholding on the frequency of phase singularity occurrence for guiding catheter ablation [3, 83, 84]. Thus, a 30×30 target output was produced for each $240 \times 240 \times 10,000$ ECP data.

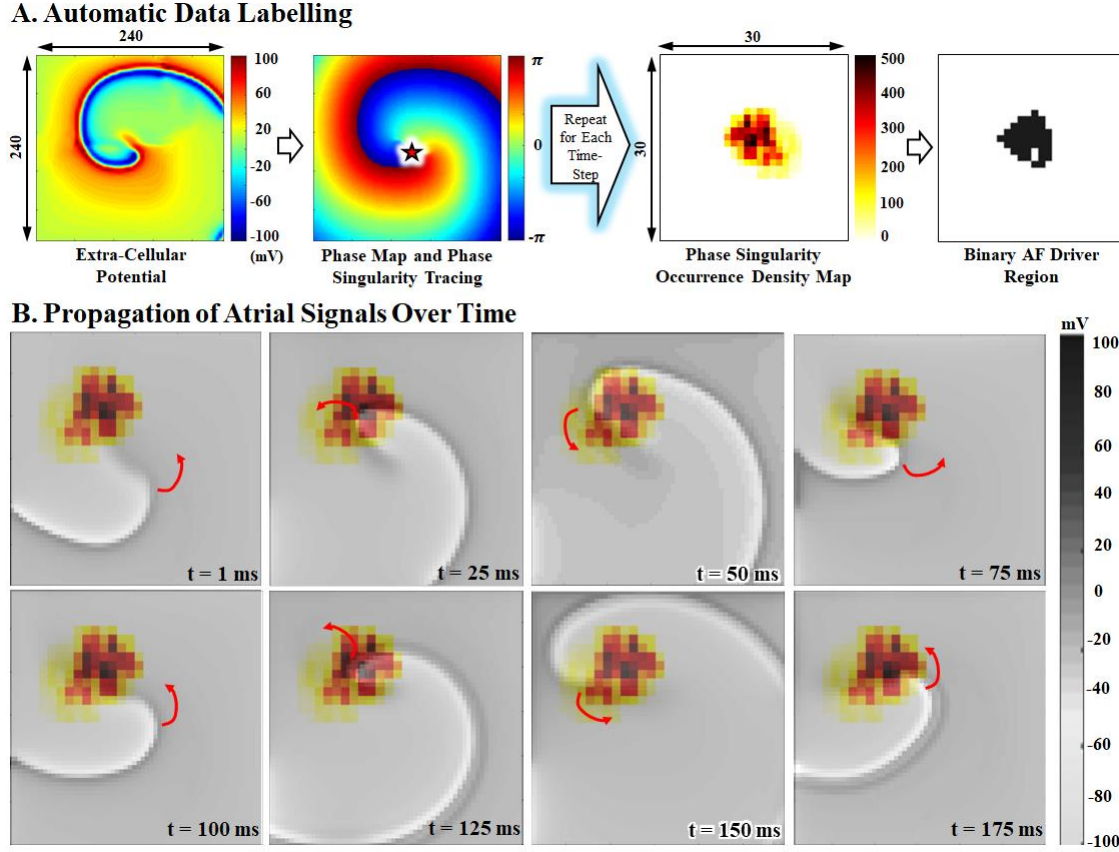


Figure 8. Generation of a 30×30 label for each $240 \times 240 \times 10,000$ extra-cellular potential (ECP) data. **A)** The ECP at each time step is converted into a phase map, and the coordinates of the phase singularity, or centroid of rotation, is identified. A density map is then created from the coordinates of the phase singularity at each time step, resulting in a frequency of occurrence map. Thresholding is used to finally to identify the region driving atrial fibrillation. **B)** The first 175ms of a typical ECP signal with the density map overlaid on top, showing the wave rotating around the AF driver region.

3.3. Convolutional Neural Networks for AF Driver Localization

AF driver identification and localization is a challenging task due to the complex propagation patterns of the atrial electrical activations, as well as the ambiguity of mechanisms sustaining arrhythmias over time in patients with AF. We propose a computational framework consisting of a novel 56-layer CNN enhanced with residual connections (**Figure 9**) to identify AF drivers from the ECP recorded from the human atria. The detailed configurations of the network architecture are provided in **Table 1**. The framework was set up such that the CNN would predict the x/y co-ordinates of the phase singularity given each ECP time step. The phase singularity predictions for all time steps of an ECP data were then concatenated to produce an aggregated density map, and 40% thresholding was used to identify the AF driver region. Each time step of an ECP signal was therefore treated as an individual data sample during training, drastically increasing the amount of training data available. Thus, the labels were the normalized x and y co-ordinates of the phase singularity at each time step produced from phase mapping.

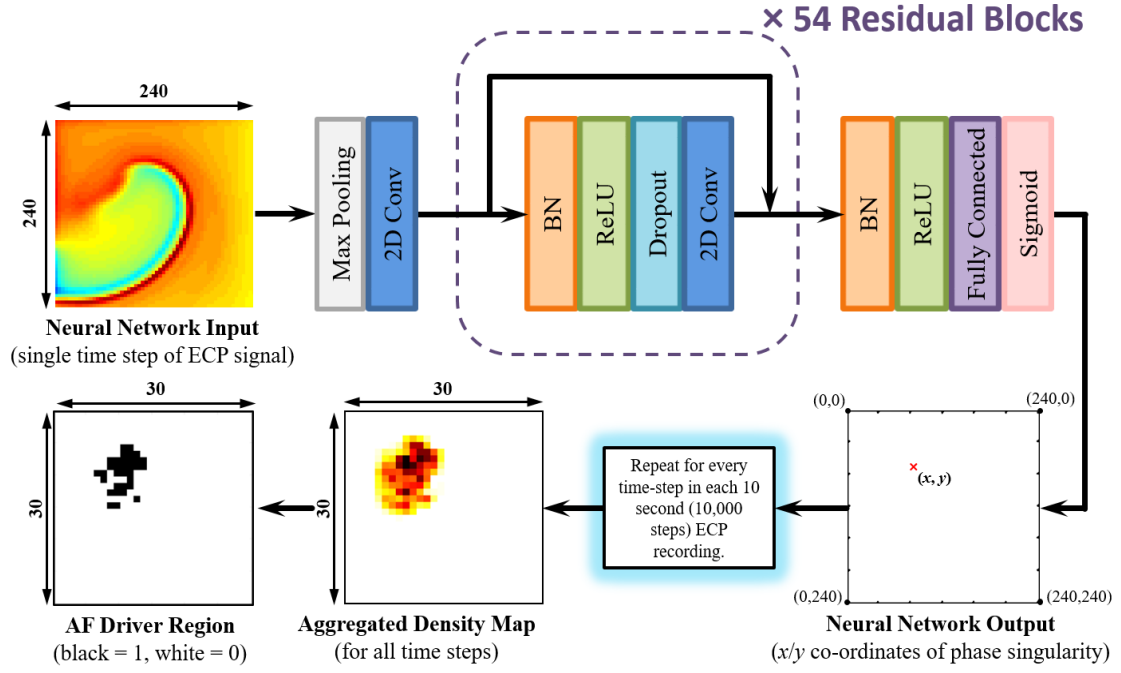


Figure 9. The architecture of the proposed 56-layer convolutional neural network for localizing AF drivers from the extra-cellular potential (ECP) over a tissue surface. The $120\text{mm} \times 120\text{mm}$ (240×240 pixels) ECP of the atrial activation patterns were fed through a single max pooling layer, a single convolutional layer, followed by 54 repeated residual blocks containing convolutions of increasing depth. The output from the residual blocks was flattened into a 1×2 vector with a fully connected layer, and the final output was the co-ordinates (x, y) of the predicted phase singularity. This was repeated for every time step of a 10 second ECP signal, resulting in 10,000 predicted locations for phase singularities which were then aggregated into a single density map. Thresholding was finally used to identify the region deemed as the AF driver. ECP, extra-cellular potential; BN, batch normalization; ReLU, rectified linear activation unit; Conv, convolutional layer; Softmax, Softmax activation function.

Table 1. The configurations of the proposed 56-layer convolutional neural network.

| Layer | Spatial Size | Filter Size | Feature Maps | Number of Parameters |
|---------------------------------|------------------------------------|--------------------------------|--------------|---|
| Input | 240×240 | - | 1 | 0 |
| Max Pooling | 60×60 | 4×4 | 1 | 0 |
| Convolution 1 | 60×60 | 3×3 | 16 | $3 \times 3 \times 1 \times 16$ |
| Convolution 2 – 19 | 60×60 | 3×3 | 16 | $3 \times 3 \times 16 \times 16 \times 18$ |
| Convolution 20 – 37 | 60×60 | 3×3 | 32 | $(3 \times 3 \times 16 \times 32) + (3 \times 3 \times 32 \times 32 \times 17)$ |
| Convolution 38 – 55 | 60×60 | 3×3 | 64 | $(3 \times 3 \times 32 \times 64) + (3 \times 3 \times 64 \times 64 \times 17)$ |
| Output (Fully Connected) | 1×2 | - | - | $3 \times 3 \times 64 \times 2$ |
| | | | | Total: 849,168 |

The CNN was composed of 55 convolutional layers with 54 residual blocks, each containing batch normalization, ReLU, dropout, and 2D convolutional layers. To decrease computational costs of the network, the 240×240 input patch was down sampled with max pooling to a 60×60 patch. This was fed through a single convolutional layer with 16 feature maps before the 54 residual blocks. The convolutional layers contained 16 feature maps in the first 18 residual blocks, 32

feature maps in the following 18 residual blocks, and 64 feature maps in the last 18 residual blocks. 3×3 filters were used to extract spatial features from the ECP in all convolutional layers as it has been shown to be the most computationally efficient and the most effective for feature learning in CNNs [85-89]. A constant dropout rate of 0.5 was used throughout the CNN to alleviate overfitting. After the residual blocks, further batch normalization and ReLU layers were used to normalize the data. Finally, a fully connected layer containing 2 nodes with a sigmoid activation was used to output the normalized x and y co-ordinates of phase singularity given each time step of an ECP signal.

The adaptive moment estimation (ADAM) optimizer [90], a type of gradient descent algorithm, was used for optimizing the weights of the CNN with the MSE objective function. The learning rate was kept constant at 0.001 without adjustment and the exponential decay rates of the 1st and 2nd-moment estimates were set to 0.9 and 0.999 respectively as suggested by previous studies [85, 86, 88]. During training, the training dataset was feed into the network in batches of 128, and the accuracy was evaluated on the validation dataset after each complete enumeration of all training data. This was repeated until the validation accuracy stopped increasing, and the best performing model was saved. The network was developed in TensorFlow [91], an open-source deep learning library for Python, and was trained on an NVIDIA Titan X-Pascal GPU with 3840 CUDA cores and 12GB RAM. The training phase took approximately 2 hours to complete, and prediction on each validation data took approximately 3 seconds.

3.4. Evaluation

CNN evaluation was performed on a subset of the generated dataset hidden during training as well as two clinical data from Stanford University [17] and University Heart Center, Hamburg [92], to determine the effectiveness of the CNN in identifying AF drivers. The F_1 score was calculated for each data in the validation set, and the overall performance was an average of individual the F_1 scores for all validation data. For each data, the F_1 score was defined for the 30×30 output as

$$F_1 = \frac{2 \times N_{true\ positive}}{\Sigma N_{ground\ truth} + \Sigma N_{predicted}} \quad (\text{Equation 12})$$

where $N_{true\ positive}$ represents the number of pixels of AF driver regions correctly identified over time for each 2D ECP, $N_{ground\ truth}$ represents the total number of pixels containing AF drivers, and $N_{predicted}$ represents the total number of pixels predicted to contain AF drivers by the model. The F_1 score has a range of [0, 1] where a larger value represented higher performance accuracies.

The MSE was also used to evaluate the performance of the CNN outputs by comparing the distance between the centroid of the predicted AF driver region and the centroid of the ground truth AF driver region. This was expected to draw out the accuracy of our approach for identifying the overall AF driver location across the atrial tissue. The MSE was measured in mm with smaller values representing higher accuracies.

3.5. Hyper-Parameter Tuning

The proposed CNN contained several hyper-parameters which were carefully selected after extensive experimentation. Various experiments were designed to evaluate the effects of different parameter values under controlled conditions on the validation set. The parameter values presented in section 3.3 of this study were, therefore, the values which yielded the highest performance during hyper-parameter tuning experiments.

Since the dimensions of the inputs directly impacted the receptive field of the proposed CNN, it was important to select a value which provided the network with sufficient information to efficiently capture features of the ECP under different atrial activation patterns. Although the 240×240 input was selected based on the human atrial physiology, the single step max-pooling layer was tuned to ensure the network sufficiently retained the relevant information while maintaining a lower number of parameters for efficient training and prediction. Since it has been shown that large CNN inputs were also prone to overfitting [93], this was an important parameter to consider as it directly impacted the feature extraction and learning stages in the rest of the network. Down-sampling factors of 1, 2, 4, 6, 8 and 10 were tested to ensure optimality of performance.

The number of residual blocks, as well as the number of feature maps for the convolutional layers within each residual block, was tuned to ensure that the selected values produced the best AF driver localization performance without using excessive computation. Experiments were first done comparing 9, 18, 36, 54, 72 and 90 residual blocks with 16 feature maps in the first 1/3 residual blocks, 32 features maps in the second 1/3, and 64 feature maps in the last 1/3 residual blocks. These specific values were selected as they were all multiples of 3 and covered a good range within the parameter search space. The number of feature maps in each residual block was then tested by comparing 8/16/32 vs 16/32/64 vs 32/64/128 feature maps throughout the network. This was expected to draw out the effects on the accuracy with the network having significantly larger or smaller number of parameters.

Overfitting was a potential issue due to the large number of layers in the proposed CNN, resulting in a large number of parameters to be optimized. To minimize this issue, dropout rates of 0%, 25%, 50% and 75% throughout the network were applied and evaluated to find the most effective number of nodes to remove while still maintaining enough nodes for sufficient feature learning. Since 0% dropout represents dropout not being applied, the effect of not applying batch-normalization was also evaluated to investigate the effects of the layer-wise normalization.

4. Results

50 ECP data with dimensions of $240 \times 240 \times 10,000$ and different reentrant circuit propagation patterns were generated for this study. This dataset was randomly split into 40 for training (80%) and 10 for validation (20%). 2 clinical data with dimensions of $240 \times 240 \times 4,000$ and $240 \times 240 \times 61,000$ and manual annotations of the AF driver regions were provided by Stanford University [17] and University Heart Center, Hamburg [94] to validate the efficacy of our approach. The clinical data were obtained with constellation basket catheters in patients with persistent AF.

4.1. Optimal Hyper-Parameters

The results of the hyper-parameter tuning experiments on the synthetic dataset are presented in this sub-section to validate the parameter choices used in our proposed CNN. **Table 2** shows the accuracy when the 240×240 input is down-sampled to different scales before the first convolutional layer. It can be seen that in the case of no pooling ($1 \times$ pooling), the network had an F_I score of 0.849 which was improved to 0.858 when the pooling factor was gradually increased to $4 \times$. Larger pooling factors greater than 4 proved to have lower accuracies. These showed that in the case of no pooling, the CNN was very prone to overfitting due to excessive input information, while in the case of very large down-sampling, the input information was insufficient for the network to effectively learn features. This also showed ECP data with a dimension less than 40×40 (as a result of $6 \times$ pooling) are not sufficient for training a CNN for AF driver localization due to the low spatial resolution.

Table 2. F_I score and Mean Squared Error (MSE) evaluation of the proposed CNN with different max-pooling factors on the 10 validation data.

| Pooling Factor | F_I Score | MSE (in mm) |
|------------------------------|------------------------------------|-----------------------------------|
| $1 \times$ | 0.849 ± 0.11 | 4.02 ± 4.04 |
| $2 \times$ | 0.851 ± 0.15 | 3.98 ± 3.95 |
| $4 \times$ | 0.858 ± 0.12 | 3.60 ± 3.50 |
| $6 \times$ | 0.832 ± 0.10 | 4.87 ± 3.56 |
| $8 \times$ | 0.804 ± 0.13 | 6.23 ± 4.15 |
| $10 \times$ | 0.756 ± 0.17 | 9.41 ± 4.89 |

Table 3 shows the performance of the proposed CNN with different numbers of residual blocks. The F_I score gradually increased as the number of residual blocks increased from 9 to 54, and the best accuracy of 0.858 was obtained from a CNN with 54 residual blocks. It can be seen that a lower number of residual blocks (<36) resulted in a network which did not contain enough parameters to effectively learn the features from the ECP data. It can also be seen that having a large number of parameters, although did not drastically decrease the performance, resulted in a network that was extremely prone to overfitting. This was also reflected in the training time and memory costs which were substantially higher for more residual blocks, showing an excess in the number of network parameters. The standard

deviation of the F_1 score of the CNN with 54 residual blocks was also the smallest, showing the best consistency during prediction.

Table 3. F_1 score and Mean Squared Error (MSE) evaluation of the proposed CNN with different numbers of residual blocks on the 10 validation data.

| Number of Residual Blocks | F_1 Score | MSE (in mm) |
|---------------------------|------------------------------------|-----------------------------------|
| 9 | 0.663 ± 0.55 | 13.24 ± 5.55 |
| 18 | 0.725 ± 0.32 | 9.98 ± 5.31 |
| 36 | 0.802 ± 0.24 | 6.21 ± 4.20 |
| 54 | 0.858 ± 0.12 | 3.60 ± 3.50 |
| 72 | 0.854 ± 0.19 | 4.01 ± 3.38 |
| 90 | 0.841 ± 0.23 | 4.76 ± 3.79 |

Once it was decided that the optimal number of residual blocks to have in the CNN was 54, the number of feature maps were tuned throughout the network. Experiments showed having 16 feature maps in residual blocks 1-18, 32 feature maps in residual blocks 19-36 and 64 feature maps in residual blocks 37-54 resulted in the best performance of 0.858. The network with 16, 32 and 128 feature maps took 5 times longer to train compared to the best performing CNN despite the relatively good accuracy of 0.847. This showed having a CNN with a moderate number of parameters is the most ideal, both for performance and computational costs.

Hyper-parameter tuning of the dropout rates throughout the network revealed 50% dropout with batch-normalization resulted in the best performance (**Table 4**). The experimental results also show that batch-normalization improves the network performance by an F_1 score of approximately 0.03, proving the importance of its inclusion. While it can be seen that dropout rates greater than 50% do not decrease the network performance drastically, dropout rates less than 50% decreases the performance of the CNN by a substantial amount, showing the importance of including sufficient dropout in the network design.

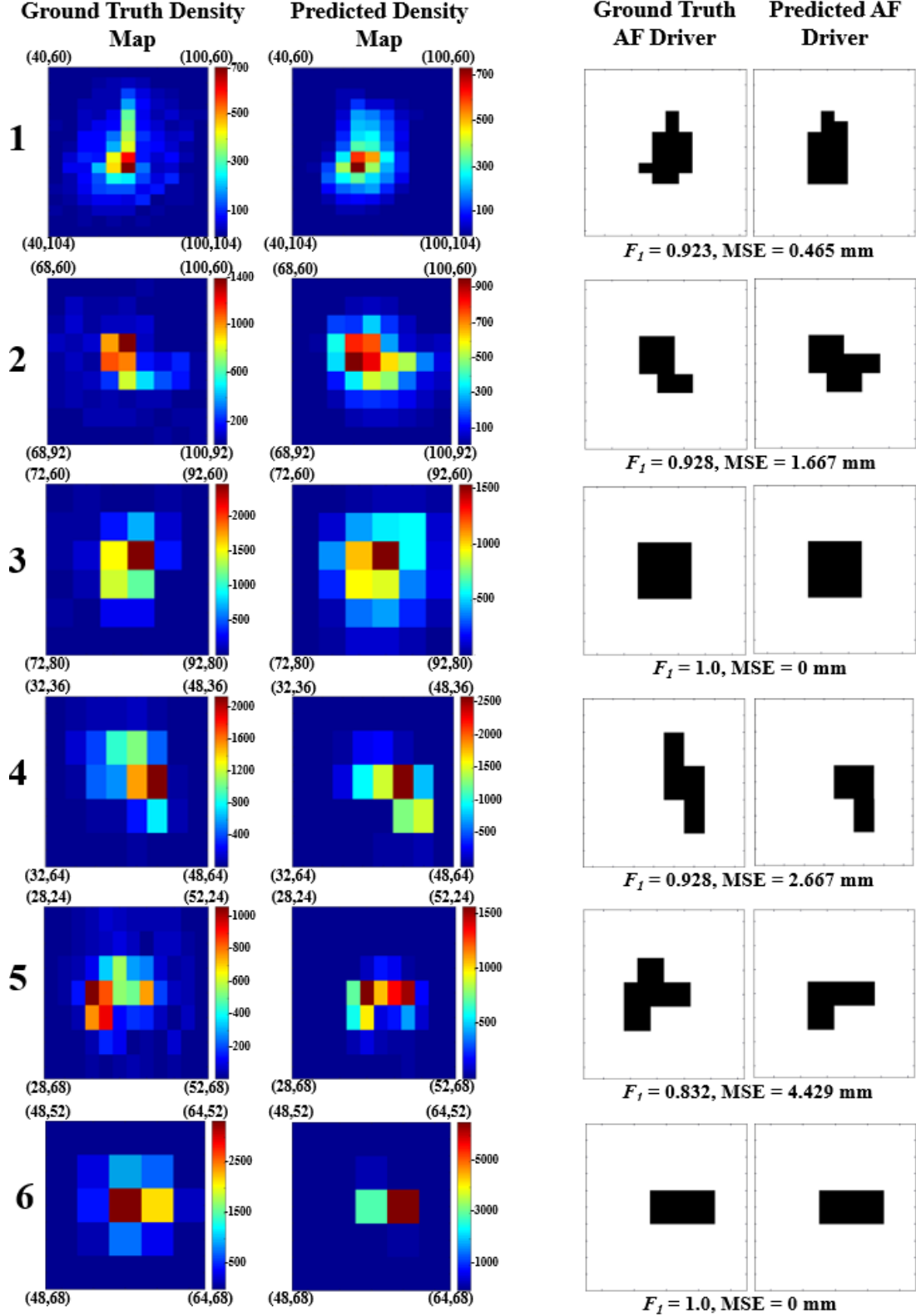
Table 4. F_1 score and Mean Squared Error (MSE) evaluation of the proposed CNN with different dropout rates with and without batch-normalization on the 10 validation data.

| % Dropout | Batch-Normalization | F_1 Score | MSE (in mm) |
|----------------|---------------------|------------------------------------|-----------------------------------|
| 0 (No Dropout) | No | 0.812 ± 0.18 | 5.97 ± 4.02 |
| 0 (No Dropout) | Yes | 0.839 ± 0.13 | 4.12 ± 3.67 |
| 25 | No | 0.825 ± 0.14 | 5.83 ± 3.78 |
| 25 | Yes | 0.855 ± 0.12 | 3.75 ± 3.33 |
| 50 | No | 0.825 ± 0.13 | 5.67 ± 3.88 |
| 50 | Yes | 0.858 ± 0.12 | 3.60 ± 3.50 |
| 75 | No | 0.821 ± 0.14 | 5.78 ± 3.91 |
| 75 | Yes | 0.856 ± 0.12 | 3.70 ± 3.28 |

4.2. AF Driver Localization Results on Synthetic Data

The proposed CNN identified AF drivers in the $120\text{mm} \times 120\text{mm}$ atrial tissue with an average F_1 score of 0.858 ± 0.12 and an MSE of $3.60\text{mm} \pm 3.50\text{mm}$ for the 10

validation data from the generated ECP dataset. **Figure 10** shows a comparison of the phase singularity frequency of occurrence density maps and the identified AF driver region after thresholding for the ground truths and predictions of the 10 validation data. Overall, our method was able to precisely localize AF drivers as the MSE showed that the CNN was on average accurate within 3.6mm of the ground truth.



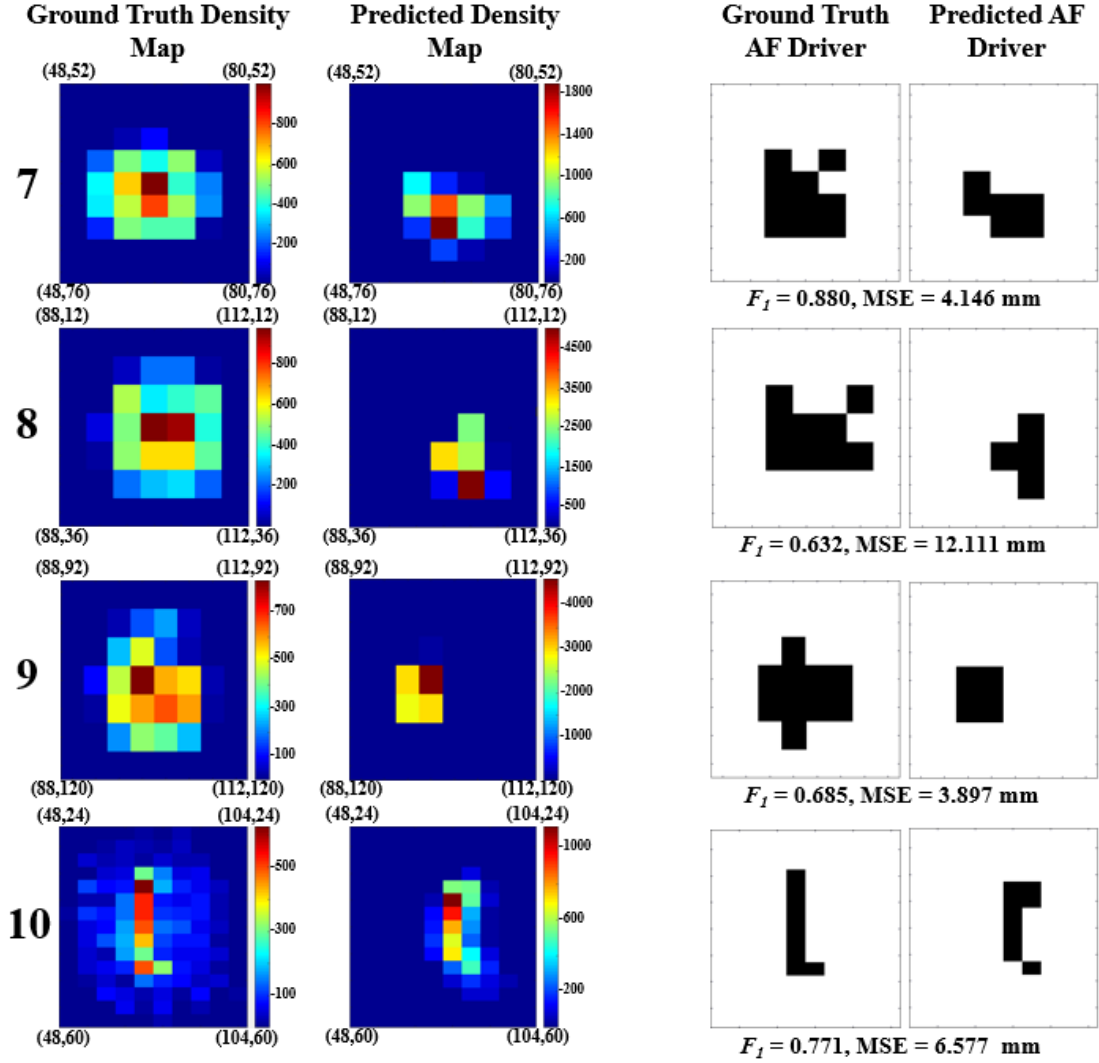


Figure 10. Comparisons of the phase singularity frequency of occurrence density maps (left) and the predicted binary AF driver region (right) for the 10 generated extra-cellular potential data in the validation set. Each row represents a single test data, where a sub-region of the entire 120mm \times 120mm atrial tissue is shown to improve the resolution. The location of the sub-region is shown with coordinates at each corner in mm. The corresponding binary maps were obtained by thresholding and the prediction accuracy for each test data is shown beneath for each data. MSE, Mean squared error.

The results show that the CNN obtained an F_1 score of above 0.90 for half the validation data (#1, #2, #3, #4 and #6) with the prediction for data #3 and #6 being 100% accurate. For these data, it can be seen that the density maps produced from the initial estimates of the phase singularity co-ordinates did not completely match the density maps generated from the ground truth singularities. However, the results after thresholding showed highly accurate predictions of the AF driver regions, most of which only contained one or two-pixel differences. For data #1 and #2, it can be seen the predictions had a tendency to overestimate the area occupied by the phase singularity over the 10-second time frame as the density maps were less concentrated in the center compared to the ground truths. This resulted in the predictions over-estimating the AF driver region. On the contrary, for data #4, the CNN

underestimated the AF driver area, as the predicted locations of the phase singularity were more concentrated towards the center. Despite these results showing the propensity of the CNN to both over or underestimate during prediction for these data, the resulting AF driver region identified was still very accurate. This was also reflected in the fact that lower MSEs did not necessarily result in higher F_1 scores which can especially be seen in data #1 and #4 which had approximately the same F_1 scores but very different MSEs.

Predictions for validation data #5 and #7 were also fairly accurate, with F_1 scores of 0.83 and 0.88 respectively. The 4.43mm and 4.15mm MSEs showed that the CNN still predicted the overall position of the driver relatively successfully. The overall areas covered by the phase singularities were predicted to be smaller than the ground truth, which could possibly explain the lower F_1 scores as a result of a smaller predicted driver region. The same can also be said about data #8, #9 and #10, in which the distribution of the phase singularity locations across the atrial tissue was predicted to be much more concentrated than the ground truth, resulting in a density map with an underestimated area. This was especially the case for data #8, for which the CNN severely underestimated the area of the density map, resulting in the predicted driver region to be 12.11 mm away from the ground truth. Interestingly, although data #9 had a very low F_1 score, the MSE was better than that of data #5 and #7 which had F_1 scores of above 0.8. This showed that although the CNN was not able to identify the pixels containing AF drivers, it was still capable of predicting the general location of the driver to a relatively accurate degree.

Overall, it can be said the most erroneous predictions stemmed from underestimating the coverage of the phase singularities within the atrial tissue which can be seen from the visualizations in **Figure 10**. The issue could potentially stem from the fact that the same thresholds are used for both the ground truth and prediction, as a threshold sufficient for the ground truth could be too high for the predictions. The high error seen in data #8 could also be attributed to the fact that the phase singularities were located near the corner of the atrial tissue, causing it to be more difficult to detect due to the lack of samples in the synthetic dataset containing reentrant circuits with their centroids very far from the center of the tissue.

4.3. AF Driver Localization Results on Clinical Data

The proposed CNN was executed on two clinical data (**Figure 11**) and obtained F_1 scores of 0.847 and 0.852 and MSEs of 5.78mm and 3.30mm (**Figure 12**). Since the data did not contain density map labels, only the predicted density map is shown for visualizing the phase singularity distribution. The predicted density maps show a clear centroid of rotation as the phase singularities were concentrated the middle of the driver region. For the Stanford data, it can be seen that the reentrant circuit followed a fairly circular path with the centroid of rotation occurring near the bottom. For the Hamburg data, it can be seen that the reentrant circuit followed an elliptical path, with the centroid occurring at exactly the center. These density maps were both fairly consistent with the ones produced from the synthetic data when visualizing the paths taken by the reentrant mechanism.

The AF driver region was underestimated for both data compared to that of the group truth, most likely due to an underestimation of the area covered by the phase singularities across the atrial tissue. This was a similar observation compared to the results on the synthetic data. The MSEs also showed a larger error compared to that of the synthetic data, suggesting that the CNN performed slightly worse on the clinical data although the overall F_1 scores were approximately the same. Nevertheless, the overall locations of the AF drivers were predicted accurate within 6mm for both clinical data, showing the approach could potentially be clinically impactful.

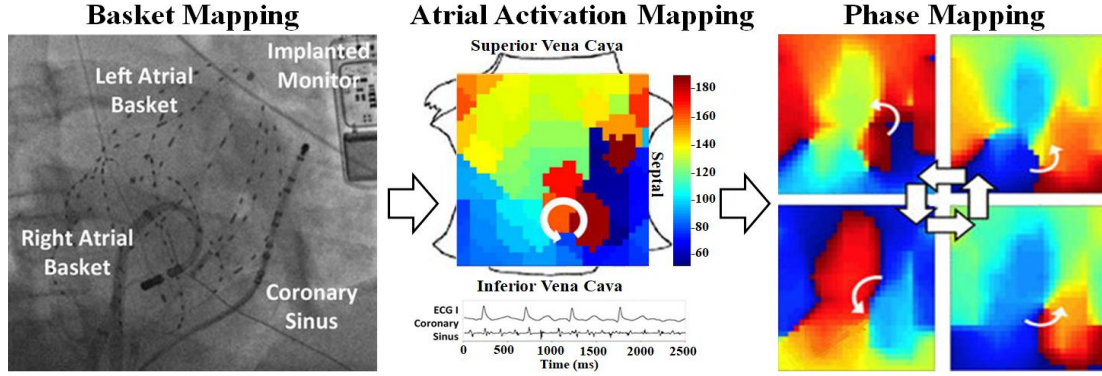


Figure 11. The recording and visualization of the clinical data from Stanford University adapted from Narayan et al. [17], demonstrating how atrial activations are typically obtained and analyzed in clinics.

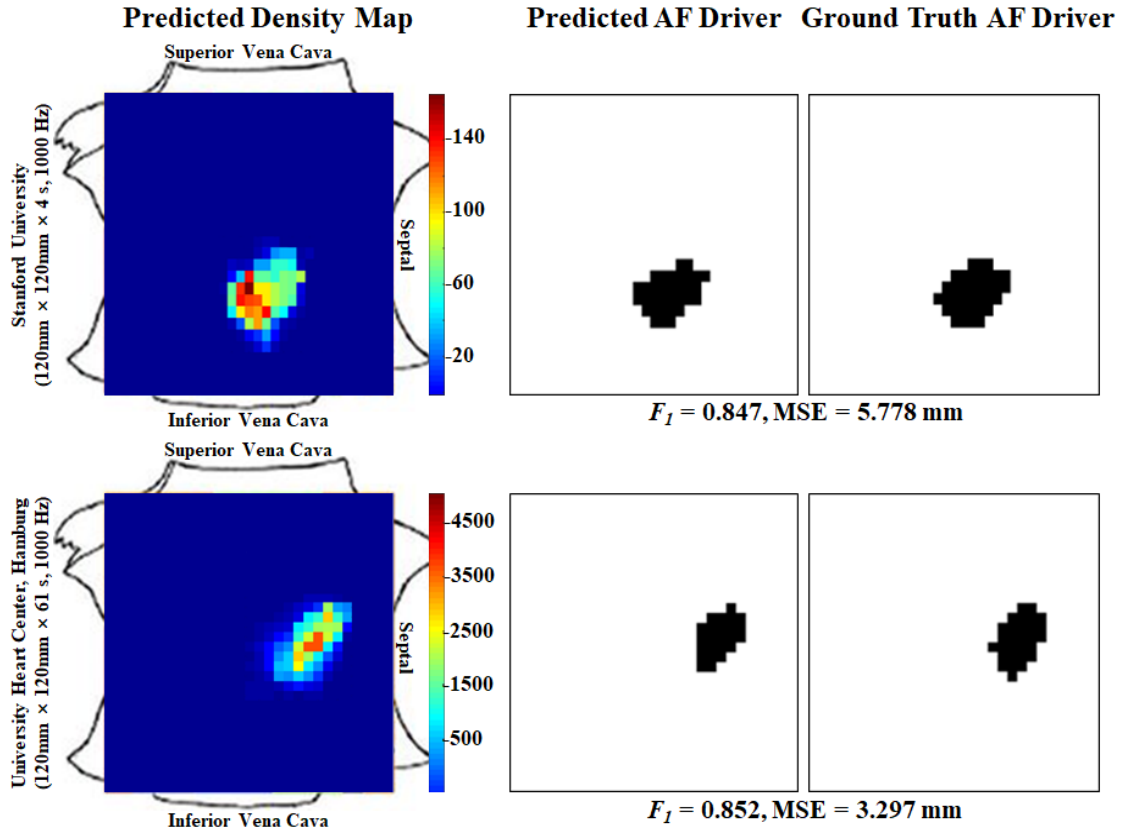


Figure 12. Comparisons of the predicted and manually annotated AF driver regions identified in the two clinical data [17, 94]. The manual annotations were performed by an expert and were kindly donated by Stanford University and University Heart Center.

5. Discussion

5.1. Algorithms for Localizing AF Drivers to Guide Catheter Ablation

Catheter ablation has been a promising clinical approach to treat patients with AF by “burning” localized atrial tissue prone to arrhythmia. Mapping devices such as constellation basket catheters have been used to visualize atrial activation patterns in real time and are used as a tool for guiding ablation treatment [4]. Tissues which trigger or sustain AF can then be identified and ablated from the patient altogether resulting in the termination of AF [95]. Thus, the ability to target problematic localized tissue accurately is the key to successful ablation.

The investigation of the key atrial regions to target during catheter ablation has been the subject of global debate. In 1998, Haïssaguerre et al. conducted a pioneering study to reveal that ectopic beats from the pulmonary veins are the key triggers of AF [32], and electrically isolating these trigger sites via ablation effectively suppressed AF. This approach, known as pulmonary vein isolation, has since been the recommended procedure for treating paroxysmal AF patients during ablation. However, successful prevention of AF recurrence remained suboptimal, as multi-center clinical trials have reported only 40-70% termination rates one year after ablation in patients with more serious AF subtypes such as persistent and permanent AF [20, 21]. The 2012 FIRM trial by Narayan et al. demonstrated the existence of localized sources in the form of reentrant circuits and focal impulses across the atrial tissue sustaining AF [17]. The study further proposed a novel computational approach for localizing and targeting these localized AF drivers to achieve extremely high success rates of 82.4% in AF termination in patients with persistent and permanent AF. Subsequent studies also reported 70-80% success rates for AF termination after a one-year follow-up using FIRM-guided ablation [18, 22]. These high percentages have therefore attracted global attention in the algorithms used in FIRM.

Despite its success, the high success rates claimed by the FIRM atrial could not be reproduced by several other independent clinical centers around the world [23, 24]. Due to the proprietary nature of the FIRM algorithm and its heavy commercialization, the details of the exact methodologies have not been confirmed and its validity has been heavily questioned. More importantly, phase mapping [96], a major component of the FIRM algorithm, has been demonstrated to introduce additional bias during analyses in the form of incomplete, “wannabe”, or false reentrant circuits [97]. Many studies have since shown that phase analysis has a propensity to over-estimate reentrant circuits by commonly misinterpreting the phase changes of linearly traveling wave-fronts [98] and rotational wave which do not complete 360-degree circuits [99] as sustained rotational drivers.

Machine learning has become increasingly popular in recent years as the methods are predominantly data-driven, alleviating potential bias introduced by assumptions with current computational approaches [82, 94, 100]. A recent 2018 study proposed the use of random forest classifiers [101] to detect AF drivers from atrial electrograms [102]. The study followed a similar workflow like the one proposed in this report, in which the model was trained on synthetic data generated from computer simulations.

However, the study outlined many limitations such as the simulated data lacking realism due to the simplified cellular models used, as well as the heavy manual feature pre-processing and selection procedure which was time-consuming. Furthermore, the study lacked clinical validation, as clinical data were not used to validate the approach. The Stanford group that led the FIRM trial also conducted a similar study in 2018 in which a CNN was developed for the purpose of identifying AF drivers entirely from clinical recordings [103]. The ECP recordings obtained from patients with AF were first transformed into phase maps. The phase maps were then broken into smaller 2D patches to train AlexNet, a CNN proposed in 2012 originally designed for image classification [26], to accurately identify whether there is an AF driver within each patch.

The computational framework proposed in this report combined the use of computer simulations and CNNs, alongside clinical validation, to produce a robust method of AF driver localization. However, our study offers several improvements over the two aforementioned studies in terms of the models used for both the data generation and machine learning. The BOCF model utilized in this study was based on physiologically and pathologically accurate human atrial cells and has been extensively shown to be capable of producing realistic atrial activation patterns [36-39]. This was reflected in the results which revealed a small difference between the validation accuracies on the synthetic data and clinical data (85.8% vs 85.0%), showing that the CNN was able to accurately predict for clinical data even though it was trained purely on synthetic data. Similar to the Stanford study, our methods involved the use of deep learning which greatly accelerated the prototyping and design stages of the development of our machine learning model. This is due to the CNN's ability to automate feature pre-processing and selection, which can often be very time-consuming and prone to bias due to the need for many human decisions [25]. Although phase mapping was used in both our study and the Stanford study, our implementation is entirely unbiased while theirs was prone to bias. This followed the arguments stated by prior literature about phase mapping having the propensity to introduce false rotational drivers due to the underlying mathematical principles of the approach [97-99]. While our study also implemented phase mapping, it was only applied to signals which were known to contain reentrant circuits since the atrial activation patterns could be precisely controlled with the BOCF model, eliminating any chance of introducing false reentries. This can be further supported by the fact that our proposed CNN was trained directly on the raw ECP signals, while the CNN proposed by the Stanford group was trained on phase maps which have been found to be overly optimistic when showing rotational sustaining AF.

The CNN proposed in this report was motivated by a groundbreaking study by He et al. in 2015 showing that the use of residual connections greatly improves optimization convergence and overfitting in large-scale CNNs [89]. While prior studies used at most 20-layer CNNs [26], the study by He et al. was the first to successfully implement CNNs with more than 50 layers to achieve state-of-the-art performances without the severe overfitting issue limiting the growth of previous CNN architectures. Since larger CNNs have greater feature learning capabilities, latter

studies have utilized residual connections to greatly enhance the performance of CNN for various challenging applications, particularly object localization tasks similar to the problem stated in this report [27, 66, 104]. The design of our methods was “end-to-end”, meaning the CNN can produce final predictions on the raw data without the need for any pre-processing [105, 106]. By setting up our computational framework in this manner, we were able to eliminate sources of bias such as phase mapping used in previously proposed methods [97]. The output of our CNN can also be easily modified to allow for the prediction of different AF sustaining mechanisms such as focal impulse or multiple wavelets by simply increasing the number of output nodes and using the same regression loss during training [27]. However, a potential point of weakness in our approach is the final step, in which thresholding was used to determine a suitable lower bound for the frequency of occurrence of the phase singularities across the atrial tissue. Although this method is commonly used in AF driver identification during clinical investigation [3, 83, 84], it could be a major source of bias as the threshold is usually chosen arbitrarily, just like in our study. Since the results showed the majority of the errors for both synthetic and clinical data were from the underestimation of the area of the AF driver region, a possible explanation could be an overly high threshold. The visualization of the density maps of the predictions vs ground truths showed that the proposed CNN was able to identify the dominant sources of rotation which were the pixels with the highest occurrence of phase singularities. However, the CNN was less successful in identifying the surrounding pixels which a much lower frequency of occurrence, showing that it is necessary to rethink the thresholding step in order to avoid underestimation of the area of the AF driver region.

5.2. Study Limitations

A major limitation when testing the efficacy of our proposed methods was the limited number of clinical data available for validation. Although large numbers of clinical recordings are currently available, the two utilized in this study were the only ones with annotations of the AF driver regions as manual labeling of atrial activation patterns is extremely time-consuming and prone to human error [2]. Other methods of automatically computing the AF driver regions with previously proposed methods are also unreliable. Hence, the clinical significance of our study remains limited as the high accuracies obtained on the two clinical data used in this study may not apply to data from other clinical centers.

Another limitation is the fact that our study only focused on investigating and identifying reentrant circuit drivers, and did not consider other potential AF sustaining mechanisms. Since the mechanisms of AF are still poorly understood, there have been many studies arguing AF is driven by non-rotational sources such as focal impulses or multiple-wavelets, which have all been claimed to be observed clinically [7]. Although the results show our proposed methods are capable of successfully identifying reentrant circuits, the accuracy when identifying other mechanisms remains to be tested, particularly on clinical data which contains such mechanisms.

The validation experiments in our study showed our proposed CNN produced

high prediction accuracies on both synthetic and clinical data. However, the CNN was only trained on 50 synthetic data which is a very small number compared to state-of-the-art CNNs which are usually trained on millions of samples. The relatively small training set used in this study could have limited the potential of the CNN to achieve higher performance scores than the values shown in this study. Hence, the effect of training the CNN with a significantly larger sample size ($>1,000,000$) remains to be investigated.

5.3. Future Work

The design of our CNN allowed for the ease of adaptation to detect other hypothesized AF sustaining mechanisms. To achieve this, computer simulations will be performed generating mechanisms of focal impulses and multiple-wavelets in order to train the CNN. The output size of the CNN would then be increased to a larger number of nodes to account for detecting the locations of different AF drivers. Since only 50 data were simulated in our study, drastically increasing the number of data to generate in future studies will greatly improve the accuracy of our approach as CNNs perform the best with large datasets. This would potentially improve the accuracy of AF driver localization making our pipeline more robust to variations in the morphology of the atrial activations in both synthetic and clinical data.

Testing a larger number of clinical data would also help to validate the efficacy of our approach for clinical applications. This would involve designing a robust process for experts to reliably annotate atrial activation patterns from multiple clinical centers, creating labels to validate our approach against. The CNN architecture could also be further improved since recent advances in deep learning have proposed more sophisticated architectures such as multiple pathways [53], feedback loops [54] and different ways to form residual connections such as nested residual blocks [86, 107] to boost the performance of CNNs. Although the architecture proposed in this study was relatively linear and efficient, more complex designs would potentially improve AF driver localization accuracies, particularly for drivers which are difficult to identify.

6. Conclusions

In this study, we have developed and evaluated a robust CNN enhanced with residual connections to perform accurate AF driver localization from atrial activation data. Our algorithm enables the identification of atrial tissue regions sustaining AF with an F_1 accuracy and MSE of 85.8% and 3.60mm for synthetic data, and 85.0% and 4.53mm for clinical data. This study is one of the first of its kind to explore the use of physiologically accurate computer simulations to accelerate deep learning for analyzing atrial activation patterns, setting a new benchmark for future studies. The methods proposed may lead to the development of more accurate approaches for targeting AF drivers during clinical ablation treatment, potentially improving clinical diagnosis and patient stratification for patients with AF. Our research findings will contribute to the international efforts in reducing AF recurrence in patients worldwide.

7. References

- [1] C. f. D. Control and Prevention, "Atrial fibrillation fact sheet," *Fact Sheets and At-a-Glance Reports*, 2010.
- [2] S. M. Narayan, M. Rodrigo, C. A. Kowalewski, F. Shenasa, G. L. Meckler, M. N. Vishwanathan, *et al.*, "Ablation of focal impulses and rotational sources: what can be learned from differing procedural outcomes?," *Current Cardiovascular Risk Reports*, vol. 11, p. 27, 2017.
- [3] M. D. O'Neill, P. Jaïs, M. Hocini, F. Sacher, G. J. Klein, J. Clémenty, *et al.*, "Catheter ablation for atrial fibrillation," *Circulation*, vol. 116, pp. 1515-1523, 2007.
- [4] B. Bencini, F. Ingle, J. Koblish, R. Tin, J. Mazzone, B. Chun, *et al.*, "Electrical mapping and cryo ablating with a balloon catheter," ed: Google Patents, 2012.
- [5] B. J. Hansen, J. Zhao, T. A. Csepe, B. T. Moore, N. Li, L. A. Jayne, *et al.*, "Atrial fibrillation driven by micro-anatomic intramural re-entry revealed by simultaneous sub-epicardial and sub-endocardial optical mapping in explanted human hearts," *European heart journal*, vol. 36, pp. 2390-2401, 2015.
- [6] J. Zhao, T. D. Butters, H. Zhang, A. J. Pullan, I. J. LeGrice, G. B. Sands, *et al.*, "An image-based model of atrial muscular architecture: effects of structural anisotropy on electrical activation," *Circulation: Arrhythmia and Electrophysiology*, p. CIRCEP. 111.967950, 2012.
- [7] J. N. Weiss, Z. Qu, and K. Shivkumar, "Ablating atrial fibrillation: A translational science perspective for clinicians," *Heart rhythm*, vol. 13, pp. 1868-1877, 2016.
- [8] S. M. Narayan and J. A. Zaman, "Mechanistically based mapping of human cardiac fibrillation," *The Journal of physiology*, vol. 594, pp. 2399-2415, 2016.
- [9] M. Haissaguerre, A. J. Shah, H. Cochet, M. Hocini, R. Dubois, I. Efimov, *et al.*, "Intermittent drivers anchoring to structural heterogeneities as a major pathophysiological mechanism of human persistent atrial fibrillation," *The Journal of physiology*, vol. 594, pp. 2387-2398, 2016.
- [10] B. Pathik, J. M. Kalman, T. Walters, P. Kuklik, J. Zhao, A. Madry, *et al.*, "Transient rotor activity during prolonged three-dimensional phase mapping in human persistent atrial fibrillation," *JACC: Clinical Electrophysiology*, 2017.
- [11] J. A. Zaman, A. S. BChir, G. G. Lalani, R. Trikha, D. E. Krummen, and S. M. Narayan, "Focal Impulse And Rotor Mapping (Firm): Conceptualizing And Treating Atrial Fibrillation," *Journal of atrial fibrillation*, vol. 7, 2014.
- [12] H. S. Lim, M. Hocini, R. Dubois, A. Denis, N. Derval, S. Zellerhoff, *et al.*, "Complexity and distribution of drivers in relation to duration of persistent atrial fibrillation," *Journal of the American College of Cardiology*, vol. 69, pp. 1257-1269, 2017.
- [13] G. K. Moe, W. C. Rheinboldt, and J. Abildskov, "A computer model of atrial fibrillation," *American heart journal*, vol. 67, pp. 200-220, 1964.
- [14] J. W. Waks and M. E. Josephson, "Mechanisms of atrial fibrillation–reentry, rotors and reality," *Arrhythmia & electrophysiology review*, vol. 3, p. 90, 2014.
- [15] E. G. Daoud, Z. Zeidan, J. D. Hummel, R. Weiss, M. Houmsse, R. Augostini, *et al.*, "Identification of repetitive activation patterns using novel computational analysis of multielectrode recordings during atrial fibrillation and flutter in humans," *JACC: Clinical Electrophysiology*, vol. 3, pp. 207-216, 2017.
- [16] S. M. Narayan, D. E. Krummen, and W. J. RAPPEL, "Clinical mapping approach to diagnose electrical rotors and focal impulse sources for human atrial fibrillation," *Journal of cardiovascular electrophysiology*, vol. 23, pp. 447-454, 2012.
- [17] S. M. Narayan, D. E. Krummen, K. Shivkumar, P. Clopton, W.-J. Rappel, and J. M. Miller, "Treatment of atrial fibrillation by the ablation of localized sources: CONFIRM (Conventional Ablation for Atrial Fibrillation With or Without Focal Impulse and Rotor Modulation) trial," *Journal of the American College of Cardiology*, vol. 60, pp. 628-636, 2012.
- [18] S. M. Narayan, T. Baykaner, P. Clopton, A. Schricker, G. G. Lalani, D. E. Krummen, *et al.*, "Ablation of rotor and focal sources reduces late recurrence of atrial fibrillation compared with trigger ablation alone: extended follow-up of the CONFIRM trial (Conventional Ablation for Atrial Fibrillation With or Without Focal Impulse and Rotor Modulation)," *Journal of the American College of Cardiology*, vol. 63, pp. 1761-1768, 2014.
- [19] G. G. Lalani, R. Trikha, D. E. Krummen, and S. M. Narayan, "Rotors and focal sources for

- human atrial fibrillation," *Circulation Journal*, vol. 78, pp. 2357-2366, 2014.
- [20] C. A. Morillo, A. Verma, S. J. Connolly, K. H. Kuck, G. M. Nair, J. Champagne, *et al.*, "Radiofrequency ablation vs antiarrhythmic drugs as first-line treatment of paroxysmal atrial fibrillation (RAAFT-2): a randomized trial," *Jama*, vol. 311, pp. 692-700, 2014.
 - [21] J. Cosedis Nielsen, A. Johannessen, P. Raatikainen, G. Hindricks, H. Walfridsson, O. Kongstad, *et al.*, "Radiofrequency ablation as initial therapy in paroxysmal atrial fibrillation," *New England Journal of Medicine*, vol. 367, pp. 1587-1595, 2012.
 - [22] J. M. Miller, R. C. Kowal, V. Swarup, J. P. Daubert, E. G. Daoud, J. D. Day, *et al.*, "Initial independent outcomes from focal impulse and rotor modulation ablation for atrial fibrillation: multicenter FIRM registry," *Journal of cardiovascular electrophysiology*, vol. 25, pp. 921-929, 2014.
 - [23] E. Buch, M. Share, R. Tung, P. Benharash, P. Sharma, J. Koneru, *et al.*, "Long-term clinical outcomes of focal impulse and rotor modulation for treatment of atrial fibrillation: A multicenter experience," *Heart Rhythm*, vol. 13, pp. 636-641, 2016.
 - [24] C. Gianni, S. Mohanty, L. Di Biase, T. Metz, C. Trivedi, Y. Gökoğlu, *et al.*, "Acute and early outcomes of focal impulse and rotor modulation (FIRM)-guided rotors-only ablation in patients with nonparoxysmal atrial fibrillation," *Heart Rhythm*, vol. 13, pp. 830-835, 2016.
 - [25] Y. LeCun, Y. Bengio, and G. Hinton, "Deep learning," *nature*, vol. 521, p. 436, 2015.
 - [26] A. Krizhevsky, I. Sutskever, and G. E. Hinton, "Imagenet classification with deep convolutional neural networks," in *Advances in neural information processing systems*, 2012, pp. 1097-1105.
 - [27] S. Ren, K. He, R. Girshick, and J. Sun, "Faster r-cnn: Towards real-time object detection with region proposal networks," in *Advances in neural information processing systems*, 2015, pp. 91-99.
 - [28] Z. Xiong, M. K. Stiles, and J. Zhao, "Robust ECG Signal Classification for Detection of Atrial Fibrillation Using a Novel Neural Network," *Computing*, vol. 44, p. 1, 2017.
 - [29] P. Rajpurkar, A. Y. Hannun, M. Haghighpanahi, C. Bourn, and A. Y. Ng, "Cardiologist-level arrhythmia detection with convolutional neural networks," *arXiv preprint arXiv:1707.01836*, 2017.
 - [30] R. Gaspo, R. F. Bosch, M. Talajic, and S. Nattel, "Functional mechanisms underlying tachycardia-induced sustained atrial fibrillation in a chronic dog model," *Circulation*, vol. 96, pp. 4027-4035, 1997.
 - [31] G. Moe and J. Abildskov, "Atrial fibrillation as a self-sustaining arrhythmia independent of focal discharge," *American heart journal*, vol. 58, pp. 59-70, 1959.
 - [32] M. Haissaguerre, P. Jaïs, D. C. Shah, A. Takahashi, M. Hocini, G. Quiniou, *et al.*, "Spontaneous initiation of atrial fibrillation by ectopic beats originating in the pulmonary veins," *New England Journal of Medicine*, vol. 339, pp. 659-666, 1998.
 - [33] S. Weidmann, "Electrical constants of trabecular muscle from mammalian heart," *The Journal of physiology*, vol. 210, pp. 1041-1054, 1970.
 - [34] B. L. Grand, S. Hatem, E. Deroubaix, J.-P. Couëil, and E. Coraboeuf, "Depressed transient outward and calcium currents in dilated human atria," *Cardiovascular research*, vol. 28, pp. 548-556, 1994.
 - [35] M. Courtemanche, R. J. Ramirez, and S. Nattel, "Ionic mechanisms underlying human atrial action potential properties: insights from a mathematical model," *American Journal of Physiology-Heart and Circulatory Physiology*, vol. 275, pp. H301-H321, 1998.
 - [36] A. Nygren, C. Fiset, L. Firek, J. Clark, D. Lindblad, R. Clark, *et al.*, "Mathematical model of an adult human atrial cell: the role of K⁺ currents in repolarization," *Circulation research*, vol. 82, pp. 63-81, 1998.
 - [37] E. Grandi, S. V. Pandit, N. Voigt, A. J. Workman, D. Dobrev, J. Jalife, *et al.*, "Human atrial action potential and Ca²⁺ model: sinus rhythm and chronic atrial fibrillation," *Circulation research*, vol. 109, pp. 1055-1066, 2011.
 - [38] M. M. Maleckar, J. L. Greenstein, N. A. Trayanova, and W. R. Giles, "Mathematical simulations of ligand-gated and cell-type specific effects on the action potential of human atrium," *Progress in biophysics and molecular biology*, vol. 98, pp. 161-170, 2008.
 - [39] J. T. Koivumäki, T. Korhonen, and P. Tavi, "Impact of sarcoplasmic reticulum calcium release on calcium dynamics and action potential morphology in human atrial myocytes: a computational study," *PLoS computational biology*, vol. 7, p. e1001067, 2011.
 - [40] A. Bueno-Orovio, E. M. Cherry, and F. H. Fenton, "Minimal model for human ventricular

- action potentials in tissue," *Journal of theoretical biology*, vol. 253, pp. 544-560, 2008.
- [41] Y. Richter, P. G. Lind, G. Seemann, and P. Maass, "Anatomical and spiral wave reentry in a simplified model for atrial electrophysiology," *Journal of theoretical biology*, vol. 419, pp. 100-107, 2017.
 - [42] C. Lenk, F. M. Weber, M. Bauer, M. Einax, P. Maass, and G. Seeman, "Initiation of atrial fibrillation by interaction of pacemakers with geometrical constraints," *Journal of theoretical biology*, vol. 366, pp. 13-23, 2015.
 - [43] F. M. Weber, A. Luik, C. Schilling, G. Seemann, M. W. Krueger, C. Lorenz, *et al.*, "Conduction velocity restitution of the human atrium—an efficient measurement protocol for clinical electrophysiological studies," *IEEE Transactions on Biomedical Engineering*, vol. 58, pp. 2648-2655, 2011.
 - [44] J. A. Suykens and J. Vandewalle, "Least squares support vector machine classifiers," *Neural processing letters*, vol. 9, pp. 293-300, 1999.
 - [45] T. K. Ho, "Random decision forests," in *Document Analysis and Recognition, 1995., Proceedings of the Third International Conference on*, 1995, pp. 278-282.
 - [46] T. Cover and P. Hart, "Nearest neighbor pattern classification," *IEEE transactions on information theory*, vol. 13, pp. 21-27, 1967.
 - [47] F. Sebastiani, "Machine learning in automated text categorization," *ACM computing surveys (CSUR)*, vol. 34, pp. 1-47, 2002.
 - [48] J. Schmidhuber, "Deep learning in neural networks: An overview," *Neural networks*, vol. 61, pp. 85-117, 2015.
 - [49] I. Goodfellow, Y. Bengio, A. Courville, and Y. Bengio, *Deep learning* vol. 1: MIT press Cambridge, 2016.
 - [50] Y. Sun, Y. Chen, X. Wang, and X. Tang, "Deep learning face representation by joint identification-verification," in *Advances in neural information processing systems*, 2014, pp. 1988-1996.
 - [51] R. Collobert, J. Weston, L. Bottou, M. Karlen, K. Kavukcuoglu, and P. Kuksa, "Natural language processing (almost) from scratch," *Journal of Machine Learning Research*, vol. 12, pp. 2493-2537, 2011.
 - [52] M. Bojarski, D. Del Testa, D. Dworakowski, B. Firner, B. Flepp, P. Goyal, *et al.*, "End to end learning for self-driving cars," *arXiv preprint arXiv:1604.07316*, 2016.
 - [53] Z. Xiong, V. V. Fedorov, X. Fu, E. Cheng, R. Macleod, and J. Zhao, "Fully Automatic Left Atrium Segmentation from Late Gadolinium Enhanced Magnetic Resonance Imaging Using a Dual Fully Convolutional Neural Network," *IEEE Transactions on Medical Imaging*, 2018.
 - [54] Z. Xiong, M. P. Nash, E. Cheng, V. V. Fedorov, M. K. Stiles, and J. Zhao, "ECG signal classification for the detection of cardiac arrhythmias using a convolutional recurrent neural network," *Physiological measurement*, 2018.
 - [55] X. Glorot and Y. Bengio, "Understanding the difficulty of training deep feedforward neural networks," in *Proceedings of the Thirteenth International Conference on Artificial Intelligence and Statistics*, 2010, pp. 249-256.
 - [56] H. Robbins and S. Monro, "A stochastic approximation method," *The annals of mathematical statistics*, pp. 400-407, 1951.
 - [57] X. Qiu, L. Zhang, Y. Ren, P. N. Suganthan, and G. Amaratunga, "Ensemble deep learning for regression and time series forecasting," in *Computational Intelligence in Ensemble Learning (CIEL), 2014 IEEE Symposium on*, 2014, pp. 1-6.
 - [58] B. Zhou, A. Khosla, A. Lapedriza, A. Oliva, and A. Torralba, "Learning deep features for discriminative localization," in *Proceedings of the IEEE Conference on Computer Vision and Pattern Recognition*, 2016, pp. 2921-2929.
 - [59] Z. Zhang, P. Luo, C. C. Loy, and X. Tang, "Facial landmark detection by deep multi-task learning," in *European Conference on Computer Vision*, 2014, pp. 94-108.
 - [60] D. E. Rumelhart, G. E. Hinton, and R. J. Williams, "Learning representations by back-propagating errors," *nature*, vol. 323, p. 533, 1986.
 - [61] D. F. Specht, "Probabilistic neural networks," *Neural networks*, vol. 3, pp. 109-118, 1990.
 - [62] V. Nair and G. E. Hinton, "Rectified linear units improve restricted boltzmann machines," in *Proceedings of the 27th international conference on machine learning (ICML-10)*, 2010, pp. 807-814.
 - [63] Y. LeCun, L. Bottou, Y. Bengio, and P. Haffner, "Gradient-based learning applied to document recognition," *Proceedings of the IEEE*, vol. 86, pp. 2278-2324, 1998.

- [64] K. Simonyan and A. Zisserman, "Very deep convolutional networks for large-scale image recognition," *arXiv preprint arXiv:1409.1556*, 2014.
- [65] C. Szegedy, W. Liu, Y. Jia, P. Sermanet, S. Reed, D. Anguelov, *et al.*, "Going deeper with convolutions," in *Proceedings of the IEEE conference on computer vision and pattern recognition*, 2015, pp. 1-9.
- [66] K. He, X. Zhang, S. Ren, and J. Sun, "Deep residual learning for image recognition," in *Proceedings of the IEEE conference on computer vision and pattern recognition*, 2016, pp. 770-778.
- [67] J. Long, E. Shelhamer, and T. Darrell, "Fully convolutional networks for semantic segmentation," in *Proceedings of the IEEE conference on computer vision and pattern recognition*, 2015, pp. 3431-3440.
- [68] H. Noh, S. Hong, and B. Han, "Learning deconvolution network for semantic segmentation," in *Proceedings of the IEEE International Conference on Computer Vision*, 2015, pp. 1520-1528.
- [69] I. V. Tetko, D. J. Livingstone, and A. I. Luik, "Neural network studies. 1. Comparison of overfitting and overtraining," *Journal of chemical information and computer sciences*, vol. 35, pp. 826-833, 1995.
- [70] N. Srivastava, G. E. Hinton, A. Krizhevsky, I. Sutskever, and R. Salakhutdinov, "Dropout: a simple way to prevent neural networks from overfitting," *Journal of machine learning research*, vol. 15, pp. 1929-1958, 2014.
- [71] Y. Bengio, P. Frasconi, and P. Simard, "The problem of learning long-term dependencies in recurrent networks," in *Neural Networks, 1993., IEEE International Conference on*, 1993, pp. 1183-1188.
- [72] S. Ioffe and C. Szegedy, "Batch normalization: Accelerating deep network training by reducing internal covariate shift," in *International Conference on Machine Learning*, 2015, pp. 448-456.
- [73] F. H. Fenton, E. M. Cherry, H. M. Hastings, and S. J. Evans, "Multiple mechanisms of spiral wave breakup in a model of cardiac electrical activity," *Chaos: An Interdisciplinary Journal of Nonlinear Science*, vol. 12, pp. 852-892, 2002.
- [74] L. E. Hudsmith, S. E. Petersen, J. M. Francis, M. D. Robson, and S. Neubauer, "Normal human left and right ventricular and left atrial dimensions using steady state free precession magnetic resonance imaging," *Journal of cardiovascular magnetic resonance*, vol. 7, pp. 775-782, 2005.
- [75] C. Schmitt, B. Zrenner, M. Schneider, M. Karch, G. Ndrepepa, I. Deisenhofer, *et al.*, "Clinical experience with a novel multielectrode basket catheter in right atrial tachycardias," *Circulation*, vol. 99, pp. 2414-2422, 1999.
- [76] Z. Qu and A. Garfinkel, "An advanced algorithm for solving partial differential equation in cardiac conduction," *IEEE Transactions on Biomedical Engineering*, vol. 46, pp. 1166-1168, 1999.
- [77] M. R. Franz, P. L. Karasik, C. Li, J. Moubarak, and M. Chavez, "Electrical remodeling of the human atrium: similar effects in patients with chronic atrial fibrillation and atrial flutter," *Journal of the American College of Cardiology*, vol. 30, pp. 1785-1792, 1997.
- [78] S. Morency, "Expandable diagnostic or therapeutic apparatus and system for introducing the same into the body," ed: Google Patents, 2003.
- [79] C. Pappone and V. Santinelli, "Multielectrode basket catheter: A new tool for curing atrial fibrillation?," *Heart Rhythm*, vol. 3, pp. 385-386, 2006.
- [80] M. Fuchs, J. Kastner, M. Wagner, S. Hawes, and J. S. Ebersole, "A standardized boundary element method volume conductor model," *Clinical Neurophysiology*, vol. 113, pp. 702-712, 2002.
- [81] S. L. Hahn, *Hilbert transforms in signal processing*: Artech House, 1996.
- [82] P. Kuklik, S. Zeemering, B. Maesen, J. Maessen, H. J. Crijns, S. Verheule, *et al.*, "Reconstruction of instantaneous phase of unipolar atrial contact electrogram using a concept of sinusoidal recomposition and Hilbert transform," *IEEE transactions on biomedical engineering*, vol. 62, pp. 296-302, 2015.
- [83] O. Wazni, B. Wilkoff, and W. Saliba, "Catheter ablation for atrial fibrillation," *New England Journal of Medicine*, vol. 365, pp. 2296-2304, 2011.
- [84] S. A. Lubitz, A. Fischer, and V. Fuster, "Catheter ablation for atrial fibrillation," *BMJ: British Medical Journal*, vol. 336, p. 819, 2008.

- [85] T. Sercu, C. Puhersch, B. Kingsbury, and Y. LeCun, "Very deep multilingual convolutional neural networks for LVCSR," in *Acoustics, Speech and Signal Processing (ICASSP), 2016 IEEE International Conference on*, 2016, pp. 4955-4959.
- [86] C. Szegedy, S. Ioffe, V. Vanhoucke, and A. A. Alemi, "Inception-v4, inception-resnet and the impact of residual connections on learning," in *AAAI*, 2017, p. 12.
- [87] Z. Wu, C. Shen, and A. v. d. Hengel, "Wider or deeper: Revisiting the resnet model for visual recognition," *arXiv preprint arXiv:1611.10080*, 2016.
- [88] C. Zhang, S. Bengio, M. Hardt, B. Recht, and O. Vinyals, "Understanding deep learning requires rethinking generalization," *arXiv preprint arXiv:1611.03530*, 2016.
- [89] K. He, X. Zhang, S. Ren, and J. Sun, "Delving deep into rectifiers: Surpassing human-level performance on imagenet classification," in *Proceedings of the IEEE international conference on computer vision*, 2015, pp. 1026-1034.
- [90] D. Kingma and J. Ba, "Adam: A method for stochastic optimization," *arXiv preprint arXiv:1412.6980*, 2014.
- [91] M. Abadi, A. Agarwal, P. Barham, E. Brevdo, Z. Chen, C. Citro, *et al.*, "Tensorflow: Large-scale machine learning on heterogeneous distributed systems," *arXiv preprint arXiv:1603.04467*, 2016.
- [92] P. Kuklik, S. Zeemering, A. van Hunnik, B. Maesen, L. Pison, D. H. Lau, *et al.*, "Identification of rotors during human atrial fibrillation using contact mapping and phase singularity detection: technical considerations," *IEEE Transactions on Biomedical Engineering*, vol. 64, pp. 310-318, 2017.
- [93] N. Srivastava, G. Hinton, A. Krizhevsky, I. Sutskever, and R. Salakhutdinov, "Dropout: a simple way to prevent neural networks from overfitting," *The Journal of Machine Learning Research*, vol. 15, pp. 1929-1958, 2014.
- [94] B. Pathik, J. M. Kalman, T. Walters, P. Kuklik, J. Zhao, A. Madry, *et al.*, "Transient rotor activity during prolonged 3-dimensional phase mapping in human persistent atrial fibrillation," *JACC: Clinical Electrophysiology*, vol. 4, pp. 72-83, 2018.
- [95] C. T. January, L. S. Wann, J. S. Alpert, H. Calkins, J. E. Cigarroa, J. B. Conti, *et al.*, "2014 AHA/ACC/HRS guideline for the management of patients with atrial fibrillation: a report of the American College of Cardiology/American Heart Association Task Force on Practice Guidelines and the Heart Rhythm Society," *Journal of the American College of Cardiology*, vol. 64, pp. e1-e76, 2014.
- [96] K. Umapathy, K. Nair, S. Masse, S. Krishnan, J. Rogers, M. P. Nash, *et al.*, "Phase mapping of cardiac fibrillation," *Circulation: Arrhythmia and Electrophysiology*, vol. 3, pp. 105-114, 2010.
- [97] R. Vijayakumar, S. K. Vasireddi, P. S. Cuculich, M. N. Faddis, and Y. Rudy, "Methodology considerations in phase mapping of human cardiac arrhythmias," *Circulation: Arrhythmia and Electrophysiology*, vol. 9, p. e004409, 2016.
- [98] S. Lee, J. Sahadevan, C. M. Khrestian, I. Cakulev, A. Markowitz, and A. L. Waldo, "Simultaneous bi-atrial high density (510-512 electrodes) epicardial mapping of persistent and long-standing persistent atrial fibrillation in patients: new insights into the mechanism of its maintenance," *Circulation*, p. CIRCULATIONAHA.115.017007, 2015.
- [99] O. Berenfeld and H. Oral, "The quest for rotors in atrial fibrillation: different nets catch different fishes," *Heart Rhythm*, vol. 9, pp. 1440-1441, 2012.
- [100] K. Shivkumar, K. A. Ellenbogen, J. D. Hummel, J. M. Miller, and J. S. Steinberg, "Acute termination of human atrial fibrillation by identification and catheter ablation of localized rotors and sources: first multicenter experience of focal impulse and rotor modulation (FIRM) ablation," *Journal of cardiovascular electrophysiology*, vol. 23, pp. 1277-1285, 2012.
- [101] A. Liaw and M. Wiener, "Classification and regression by randomForest," *R news*, vol. 2, pp. 18-22, 2002.
- [102] M. F. McGillivray, W. Cheng, N. S. Peters, and K. Christensen, "Machine learning methods for locating re-entrant drivers from electrograms in a model of atrial fibrillation," *Royal Society open science*, vol. 5, p. 172434, 2018.
- [103] J. A. Zaman, W. H. Sauer, M. I. Alhusseini, T. Baykaner, R. T. Borne, C. A. Kowalewski, *et al.*, "Identification and characterization of sites where persistent atrial fibrillation is terminated by localized ablation," *Circulation: Arrhythmia and Electrophysiology*, vol. 11, p. e005258, 2018.
- [104] R. Girshick, J. Donahue, T. Darrell, and J. Malik, "Rich feature hierarchies for accurate object detection and semantic segmentation," in *Proceedings of the IEEE conference on computer*

- vision and pattern recognition*, 2014, pp. 580-587.
- [105] A. Hannun, C. Case, J. Casper, B. Catanzaro, G. Diamos, E. Elsen, *et al.*, "Deep speech: Scaling up end-to-end speech recognition," *arXiv preprint arXiv:1412.5567*, 2014.
 - [106] D. Amodei, S. Ananthanarayanan, R. Anubhai, J. Bai, E. Battenberg, C. Case, *et al.*, "Deep speech 2: End-to-end speech recognition in english and mandarin," in *International Conference on Machine Learning*, 2016, pp. 173-182.
 - [107] J. Hu, L. Shen, and G. Sun, "Squeeze-and-excitation networks," *arXiv preprint arXiv:1709.01507*, vol. 7, 2017.